Microstructure - Property Correlation

P-54

a research project

under grant NAG 3-506

funded by

NASA-Lewis Research Center
Cleveland, Ohio

Final report

submitted by

N. Jayaraman
Professor of Metallurgical Engineering
Department of Materials Science and Engineering
University of Cincinnati
Cincinnati, Ohio 45221-0012.

October 1, 1990

Background:

The subject grant no. NAG 3-506 was initiated in December 1983 and ended on January 1990. During this period, with the support of this grant several small research projects were carried out and a number of undergraduate and graduate students of the Department of Materials Science and Engineering, University of Cincinnati were trained at NASA Lewis Research Center under the supervision of various scientists. The research work was conducted at the University of Cincinnati by the some of the students under the supervision of the P.I. The following students were involved in these activities:

1. Walter W. Milligan - Senior Project thesis, 1983-84 - (NASA Advisor : Dr. Robert C. Bill)
2. Kevin Hemker - Senior Project thesis, 1984-85 (NASA Advisor: Dr. Robert V. Miner)
3. Dan Thoma - Senior Project thesis, 1985-86 (NASA Advisor: Mr. Thomas Glasgow)
4. Pete Kantzos - Summer student at NASA-Lewis Research Center, 1985 (NASA Advisor: Mr. Jack Telesman and Dr. Marv Hirschberg)
5. David Lee - Summer student at NASA-Lewis Research Center, 1985 (NASA Advisor: Dr. Hugh Gray)
6. Frank Ritzert - Summer student at NASA-Lewis Research Center, 1986 (NASA Advisor: Dr. Hugh Gray)
7. Vijay Ramakrishnan - Graduate student training at NASA-Lewis Research Center, Winter 1989(NASA Advisor: Dr. Brad Lerch)
8. Thomas E. Fetsko - Graduate student training at NASA-Lewis Research Center, 1988-90 (M.S. degree awarded: 1990; NASA Advisor: Dr. Ram T. Bhatt).
9. Monika Ditmars - Graduate student at the University of Cincinnati, 1984-86 (M.S. degree awarded: 1987)
10. Jun Sonu - Graduate student at the University of Cincinnati, 1984-88 (Ph.D. degree awarded: 1988)

Results from these research work have been presented at various NASA meetings, National and international conferences and some of these work have also been published as journal articles. This report summarizes some of the important results from two of the very recent projects completed under this program:

Multiaxial fatigue damage evolution in waspaloy:

ABSTRACT

Strain controlled torsional and biaxial (tension-torsion) low cycle fatigue behaviour of Waspaloy was studied at room temperature as a function of heat treatment. Biaxial tests were conducted under proportional (when the axial and torsional strain cycles are in-phase) and non-proportional (when the axial and torsional strain cycles are 90^{o} out-of-phase) cyclic conditions. The deformation behaviour under these different cyclic conditions were evaluated by slip trace analysis. For this, a Schmidt-type

factor was defined for multiaxial loading conditions and it was shown that when the slip deformation is predominant, non-proportional cycles are more damaging than proportional or pure axial or torsional cycles. This was attributed to the fact that under non-proportional cyclic conditions, deformation was through multiple slip as opposed single slip for other loading conditions, which gave rise to increased hardening. The total life for a given test condition was found to be independent of heat treatment. This was interpreted as being due to the differences in the cycles to initiation and propagation of cracks.

1. INTRODUCTION

Aircraft engine components are often subjected to complex multi-axial cyclic stresses. Plastic deformation behaviour under multi-axial stress state is different from that observed under uniaxial conditions (1-4). In this paper the plastic deformation aspects of multiaxial fatigue is considered. Waspaloy was chosen for this study since its uniaxial fatigue behaviour was extensively studied in an earlier study (5).

Lerch, Jayaraman and Antolovich (5) examined the uniaxial low cycle fatigue (LCF) behaviour of Waspaloy. Two different heat treatments and therefore, two different microstructures were examined, namely heat treatment A to produce a microstructure consisting of fine grain size (ASTM G.S.#9) with large gamma prime prcipitate particles (about 900 A diameter) and heat treatment F to produce a microstructure consisting of coarse grain size (ASTM G.S.#3) with small gamma prime precitate particles (about 50-80 A diameter). Although under strain controlled fatigue testing both these microstructures gave relatively similar total lives, for heat treatment A most of the life was spent in crack initiation and the plastic deformation was uniformly distributed by the Orowan looping mechanism. As opposed to this, for heat treatment F, most of the fatigue life was spent in propagation of cracks initiated earlier, and the deformation was localized in slip bands formed due to precipitate shearing mechanism.

In this paper, again Waspaloy with the above two microstructures was tested for the torsional and biaxial (tension-torsion) LCF behaviour. Biaxial fatigue studies where the tension and torsional cycles were in-phase and where the two were 90° out-of-phase were conducted. The main purpose of these studies was to illustrate the slip and deformation processes, and fatigue fracture in the different types of biaxial fatigue conditions.

2. MECHANICS OF BIAXIAL FATIGUE

2.1. Schmidt factor calculations for slip

Biaxial LCF testing in this study was accomplished by cyclically applying torsional and axial strains to a tubular sample. Both cycles were applied at the same frequency. A

biaxial test is said to be in-phase, or proportional, when σ/τ or ϵ/γ = constant. It is said to be out-of-phase, or non-proportional when there is a phase shift between the axial and torsional cycles. Figure 1 demonstrates the difference between in- and 90^{o} out-of-phase fatigue cycles. Note that purely axial and purely torsional tests are proportional.

When a sufficient stress or a combination of stresses is applied to a metallic material, plastic deformation occurs. On a microstructural level, this deformation is caused by the motion of dislocations (slip). In face centered cubic materials, slip tends to occur usually in the twelve possible octahedral slip systems (denoted by {111}<110>). For any given state of stress, slip is most likely to occur on those slip systems with the greatest resoved shear stress.

In the most general case the resolved shear stress can be determined as follows (6):

$$\tau_{RSS} = \begin{matrix}\phi_1 & \phi_2 & \phi_3\end{matrix} \begin{matrix}\sigma_{xx} & \tau_{xy} & \tau_{xz} \\ \tau_{yx} & \sigma_{yy} & \tau_{yz} \\ \tau_{zx} & \tau_{zy} & \sigma_{zz}\end{matrix} \begin{matrix}\delta_1 \\ \delta_2 \\ \delta_3\end{matrix} \qquad \ldots (1)$$

where ϕ is the unit vector in the direction of the slip plane normal, δ is the unit vector in the slip direction and σ_{ij} is a stress tensor describing the state of stress at the point under consideration. For the case of the simple uniaxial stress, this equation reduces to a more familiar form as follows:

$$\tau_{RSS} = \sigma \text{ Cos } \phi \text{ Cos } \delta \qquad \ldots (2)$$

which is the Schmidt equation. The term Cos ϕ Cos δ is the Schmidt factor and has a maximum possible value of 0.5.

For the more complex biaxial case also, Schmidt-type factors can be determined. For tension-torsion loading the Schmidt factor has been shown to be (7):

$$\frac{\tau_{RSS}}{(\sigma^2 + 4\,\tau^2)} \qquad \ldots (3)$$

where σ = applied axial stress, and
τ = applied shear stress.

The biaxial Schmidt factor also has a maximum possible value of 0.5.

2.2. Planes of Maximum Shear

For any given stress state, the axes of principle stresses and the planes of maximum shear stress can be uniquely determined by using standard tensor algebra (6). It can easily be demonstrated (7) that for a cylindrical or tubular body stressed by any combination of axial and torsional loads that two of the axes of principle stresses lie on (or parallel to) the plane tangent to the surface of the body at any point on its circumference. The third principle stress is normal to the surface and always has a value of zero. The maximum shear stress acts on a plane whose normal bisects the angle between the directions of the largest and smallest principle stresses. The planes of maximum shear is therefore perpendicular to the surface of the body at all points (figure 2) and their orientation with reference to the sample axis has been shown to be (8):

$$\tan 2\theta = \frac{-\sigma}{2\tau} \qquad \ldots (4)$$

where θ is the angle between the specimen axis and the plane of maximum shear.

Under pure axial or pure torsional cyclic loading the orientations of both the principle axes and the maximum shear planes remain fixed with respect to the sample during the course of each cycle. For pure axial loading the maximum shear planes can be shown from equation 4 to be at angles of 45^{o} and 135^{o} to the specimen axis and for pure torsional loading these planes are parallel and perpendicular to the sample axis. This means that the Schmidt factors for various slip systems do not vary during fatigue testing unless the crystal itself rotates. In other words, the resolved shear stress will always be greatest on one slip system (or possibly several systems if the Schmidt factors on these are identical).

Figures 3a and b demonstrate how the resolved shear stress on the twelve possible slip systems varies during on axial and one torsional fatigue cycle, respectively. The applied load was varied sinusoidally for these examples and the cycle begins and ends at zero load. The crystal in these examples was arbitrarily chosen to have a single slip orientation of [158] for the specimen axis and $[7\bar{3}1]$ with respect to the surface normal. Notice in these figures that one slip system always has the maximum shear stress at all times during the cycle.

During a biaxial fatigue cycle, the principle axes and therefore maximum shear planes maintain a fixed orientation if and only if the loading is proportional, i.e., σ/τ = constant at all points during the fatigue cycle. For example, for the test conditions of this study, the orientation of the maximum shear planes were determined using equatin 4 to be at fixed angles of 30^{o} and 120^{o} with reference to the sample axis. Figure 3c shows how the resoved shear stress varies on the twelve slip systems

for a proportional biaxial fatigue cycle. Notice again, that only one slip system has the largest resolved shear stress value at all times during the cycle.

If the loading is non-proportional, the principle axes and therefore the maximum shear planes will rotate with respect to the crystal by 180^{o} in the course of each cycle. Figure 3d shows how the resolved shear stress on the twelve slip systems varies during a 90^{o} out-of-phase cycle. Notice that now several slip systems share the privilege of having the greatest resolved shear stress during various portions of the cycle. Under these circumstances, extensive multiple and/or cross slip is highly possible.

In this paper, it is shown that the above analysis is very consistent with the observed slip and hardening behavior of Waspaloy subjected to torsional and biaxial (both proportional and non-proportional) fatigue.

3. EXPERIMENTAL

3.1 Materials and Heat Treatments

A Waspaloy billet was supplied by Cyclops Cytemp Specialty Steel Division. The chemical composition of the billet is listed in Table I. The 55cm X 50cm X 5cm billet was hot rolled at $1230^{o}C$ to approximately 100cm X 50cm X 3.2cm. The final hot rolling was done in the 100 cm direction. The plate used in the previous investigation(5) was cross rolled to its final dimensions. As will be shown later, this final hot rolling did not introduce any significant anisotropy in the grain structure of the billet.

Specimens were heat treated in air, in a resistance-type furnace. The heat treatments were the same as those used in the previous investigation(5). Details about the heat treatment and the microstructures can be found in reference (5). For the sake of completeness these are summarized in Table II and discussed briefly in Section 4.

3.2. Mechanical Testing

3.2.1. Specimen Configuration

Longitudinal LCF specimens with a hollow cylinder configuration were machined from the billet with their long axis parallel to the final rolling direction. An outer diameter (o.d.) to wall thickness ratio of 10:1 was chosen to facilitate stress calculations. With this ratio, the specimen can be considered to be thin walled and the stresses can be assumed to remain the same through the wall thickness. Figure 4 shows the specimen geometry. The central bore was gun-drilled and honed to a 16 micron rms (root mean square) finish. The outside surface was low stress ground and polished to a 8 micron rms. In addition, all the specimens were also electropolished on the outside

surface and examined under a low power optical microscope for any surface scratches or damage.

3.2.2. Fatigue Testing

Fatigue tests were performed at room temperature on a closed loop servohydraulic biaxial (tension-torsion) MTS machine interfaced with an LSI 11-23 computer. This computer was used for test control, data acquisition and analysis. All tests were strain controlled and fully reversed. Strains were detected by a previously calibrated MTS biaxial extensometer. The calibration procedures are detailed in reference (7). The extensometer is capable of measuring axial displacements and torsional rotations simultaneously. The load cell is capable of measuring both axial loads and torques. Therefore the axial stress and strains could be determined from the axial load and displacement. Since the torsional strain varies linearly with radius, whether the deformation is elastic or plastic, $c = rv/L$, where c is the torsional strain, v is the angle of twist, r is the radius and L is the gage length of the sample. Torsional stress is however, somewhat more complex to determine, because the relationship between stress and radius can not be defined in the plastic region. For this purpose, a thin-walled tube with an o.d. to wall thickness ratio of atleast 10:1 was chosen for the specimen configuration. Then assuming that the torsional stress is the same through the thickness of the tube (8)

$$\tau = \frac{3T}{2\pi (r_0^3 - r_i^3)} \qquad \ldots (5)$$

where T is torque and r_0 and r_i are the outer and inner radii of the tube respectively.

Torsional, in-phase tension-torsion and 90^o out-of-phase tension-torsion tests were conducted for both heat treatments. Since plastic strain controlled (constant De_p) uniaxial LCF tests were conducted in the earlier investigation (5), about half of the tests in the present work were done under constant plastic strain range. In order to accomplish this, the total strain range was continuously adjusted during the strain controlled tests. This technique worked well for the torsional and the in-phase biaxial tests. However, in the 90^o out-of phase biaxial tests, the definitions of axial and torsional plastic strains are not clear. For this reason ten of the twenty three tests were run under total strain control. As shown later, the test results from these two different types of tests showed similar trends and therefore could be analyzed by the same analytical methods. All fatigue tests were run to failure, which was defined as a sharp drop in the tensile load amplitude (for biaxial tests) or the

shear load amplitude (for torsion tests). Physical observation showed that this sharp drop corresponded with the development of a rapidly propagating macrocrack. No special effort was made to detect the moment of crack initiation.

3.3. Metallography

3.3.1. Optical Metallography

The following three different optical metallography techniques were used to examine selected test specimens:
(i) Macrophotography of the crack,
(ii) Microphotography of the gage surface, without any surface preperation of the test specimen, and
(iii)Microphotography of the mounted, polished and etched sections of the tested samples. Details of the procedures can be found in reference (7).

3.3.2. Scanning Electron Microscopy (SEM)

Fracture surfaces of selected specimens were examined by SEM to characterize the fracture mode and propagation behaviour. The gage surface was also examined for secondary cracking and slip band formation.

4. RESULTS AND DISCUSSION

4.1. Material Characterization

4.1.1. Grain Size

The grain sizes were determined by the Heyn intercept method given in ASTM Standard E112 (10). Heat treatment A (with a solutionizing temperature of 1010^{o}C) was found to have a grain size of ASTM size 7 (approximately 32 microns). No grain growth took place during the 1010^{o}C solution heat treatment. Heat treatment F (with a solutionizing temperature of 1030^{o}C)had a grain size of ASTM size 2 (approximately 180 microns). The grain sizes of the two heat treatments used in this investigation are slightly larger than those used in the earlier work (5) and this is due to the difference in the grain sizes of the as-received billets in the two studies. In reference(5), the starting billet had an ASTM size of 9-10 as opposed to an ASTM size of 7 in this work. As shown later, this small difference in the grain sizes did not significantly affect the results. Thus, as in the previous study, the two heat treatments were designed to give a fine and a coarse grain structure.

4.1.2. Gamma Prime Phase

The aging heat treatments (for both A and F) were designed to produce large and small gamma prime precipitate particles respectively, which in turn can affect the deformation mode (i.e., either looping or shearing) and hence the damage mechanisms. Accordingly, heat treatment A produced a duplex gamma prime structure with particle sizes of 900 and 3000 A. The

larger particles were unsolutionized and therefore grew during aging. Heat treatment F produced a small gamma prime structure with particles in the size range of 50-100 A. High resolution darkfield transmission electron microscopy (TEM) images of the precipitates for both heat treatments are shown in figure 5. These results are in agreement with those previously reported(5).

4.1.3. Carbides

As in the previous study (5), the fine grained material (heat treatment A) showed discrete carbide particles at or near grain boundaries while the coarse grained material (heat treatment F) showed an absence of grain boundary carbides. Figure 6 shows SEM photographs of typical grain boundaries from these heat treatments.

4.2. Low Cycle Fatigue Test Results

All the fatigue test results are summarized in Table III. The experimental parameters such as $\Delta\epsilon$, $\Delta\gamma$, etc., were determined at $N_f/2$, where N_f is the number of cycles to failure which, as indicated earlier, was determined by the sudden drop in the axial load (for biaxial tests) and torsional loads (for torsion fatigue tests). The analyses of life from these test results are discussed in another paper (11). Here, only the deformation characteristics, the cyclic hardening behaviour and the fracture characteristics will be discussed.

4.2.1. Hysterisis Loops

Figures 7a-e show typical hysterisis loops (stress vs. strain plots for one cycle) from torsional, biaxial in-phase and biaxial 90^o out-of-phase tests. The biaxial tests have two hysterisis loops, one for axial and another for torsional. The torsional test loops and the biaxial in-phase test loops are very similar to the ones obtained in uniaxial tests. These loops characteristically show a linear elastic region followed by a non-linear plastic region, indicating that there are periods of time when the material experiences only elasic strains (or stresses). As opposed to this, the biaxial 90^o out-of-phase test loops (figures 7d and e) bear little resemblance to their in-phase counterparts. Similar loops have been reported by other researchers (1) and predicted by constitutive models (12). The unusual shape of the loops can be attributed to the fact that at no time does the material undergo elastic deformation. Notice that there are still linear regions in these loops. These can not however be considered elastic regions, since their slopes do not equal the elastic modulus (or the shear modulus) of the material. For both the torsional and biaxial in-phase loops, one can easily identify the plastic strain ranges by conventional methods from the loop widths. However, for the 90^o out-of-phase tests, because there are no elastic regions, the loop width is only remotely related to the plastic strain. For this reason, the plastic strain control method was abondoned in favour of a

total strain control method for the remaining ten tests. These are appropriately indicated in Table III.

4.2.3. Cyclic Hardening Behavior

Figures 8a-e and figures 9a-e show the cumulative glide paths (stress vs. number of cycles) for both heat treatments A and F respectively. Experimental results from pure torsion and biaxial, proportional and non-proportional fatigue tests are presented in these plots. Since both axial and torsional stresses were monitored during biaxial tests, the corresponding cumulative glide plots are shown. As seen in these figures, the general hardening-softening behaviour is similar to that seen in the uniaxial LCF studies(5), namely, heat treatment F showed fairly rapid hardening and softening to failure. In contrast, the heat treatment A showed slow hardening and little softening. Non-proportional biaxial fatigue cycles tended to harden more than proportional biaxial fatigue cycles or torsional fatigue cycles. It will be shown that this additional hardening is the result of multiple slip. The relative hardening behaviors for the torsional, biaxial proportional and the biaxial non-proportional fatigue cycles are consistent with the slip deformation analysis discussed in Section 2.

4.2.4. Deformation Analyses

Figures 10a-f show typical optical micrographs of polished and etched sections of test samples. These micrographs show the orientation of slip bands with refernce to the sample axis (the horizontal axis in the micrographs). Figures 10a and b show the micrographs of samples of heat treatment A and F respectively, tested in pure torsion. The planes of maximum shear stress in a torsional fatigue sample, as shown previously in section 2, are parallel and perpendicular to the sample axis. Note that all the slip bands are either parallel or perpendicular to the sample axis. Figures 10c and d are the micrographs for typical biaxial proportional tests. Again, the slip traces seen in these figures are oriented approximately at 30^{o} and 120^{o} to the specimen axis, and this was as predicted in section 2. Figures 10e and f are micrographs for typical non-proportional biaxial tests. As predicted in section 2, the maximum shear planes rotate continuously, and therefore, many slip systems become active during fatigue cycles. The above descriptions are generally true for both heat treatments, but is immediately obvious in heat treatment F, because of the larger grain size.

Figures 11a-f show macrophotographs and schematic of sample surfaces with the primary cracks. Again, these crack orientations are very consistent with the proposed deformation modes in Section 2. For example, in pure torsion, the primary crack is either perpendicular or parallel to the axis of the sample, thus confining to the maximum shear planes (figures 11a and b). Likewise, for the proportional biaxial test, the crack is again located on the maximum shear planes (figures 11c and d).

For the non-proportional biaxial tests, the crack is snake shaped (figures 11e and f), thus not confining to any specific plane, which is consistent with earlier discussions. In all these cases, the initial mode II type crack (formed by shear) changes to mode I type crack as crack extension takes place. Microcracks on the tested sample surfaces were observed in both heat treatments, though more frequently in heat treatment A. These microcracks were preferentially on the maximum shear planes. Typical example of microcracks in a tested sample is shown in figure 12. Fractography of the fracture surfaces indicated that the crack propagation in these materials is by classical striation mechanism. Typical example of the striations is shown in figure 13.

5. SUMMARIZING REMARKS AND CONCLUSIONS

Torsional and biaxial (tension-torsion) fatigue tests of Waspaloy were conducted to illustrate the importance of metallurgical and microstructural aspects of multiaxial fatigue. Waspaloy, in two heat treatments, was tested for its torsional and biaxial (tension-torsion) fatigue behavior. The results indicate that slip deformation and cyclic hardening are dependent upon the type of fatigue test. For example, biaxial out-of-phase (non-proportional) tests were found to be more damaging than biaxial in-phase (proportional) tests and torsional tests. This is due to the differences in the associated slip deformation. Uniaxial, torsional and proportional biaxial fatigue were shown to usually exhibit single slip deformation mechanisms and non-proportional biaxial fatigue was shown to exhibit multiple slip deformation. The slip deformation aspect of multiaxial fatigue is important only at low temperatures. At high temperatures, other metallurgical effects such as creep damage and environmental effects will have significant influence on the multiaxial fatigue behaviour.

The need for defining the test parameters for biaxial tests has also been highlighted during the course of this work. For example, the conventional definition of plastic strain range, as defined by the width of the hysterisis loop for uniaxial fatigue, is not any more true for non-proportional multiaxial fatigue.

ACKNOWLEDGEMENTS

The authors gratefully acknowledge the financial support of the NASA Lewis Research Center, National Aeronautics and Space Administration, under grant NSG 3 506. We would also like to thank John L. Milavec of Cyclops Corporation's Cytemp Specialty Steel Division for generously supplying the material.

REFERENCES

(1) K. Kanazawa, K.J. Miller and M.W. Brown, Fatigue of Engineering Materials and Structures,Vol.2,(1979) pp217-228.
(2) H.S. Lamba and O.M. Sidebottom, Journal of Engineering Materials and Technology, Vol. 100, (1978) pp96-103.

(3) E. Krempl and H. Lu, Journal Engineering Materials and Technology, Vol.106, (1984) pp 376-382.
(4) C.M. Sonsino and V. Grubisic, Multiaxial Fatigue, ASTM STP 853, (1985) pp 586-605.
(5) B.A. Lerch, N. Jayaraman and S.D. Antolovich, Materials Science and Engineering, Vol. 66, (1984) pp 151-166.
(6) W. Lai and E. Saibel, Elements of Mechanics of Elastic Solids, Addison-Wesley Publishing, 1965.
(7) M.M. Ditmars, M.S.Thesis, University of Cincinnati,1987.
(8) F.P. Beer and E.R. Johnston, Mechanics of Materials, McGraw Hill Publication, 1981.
(9) M.W. Brown, Journal of Strain Analysis for Engineering Materials, Vol.13, (1978), pp 23-28.
(10) ASTM E112-88,"Standard Test Methods for Determining Average Grain Size", Annual Book of Standards, American Society for Testing Materials, Vol 03.01. Section 3, Philadelphia, 1989.
(11) J. Sonu, M.M. Ditmars and N. Jayaraman, paper to appear in International Journal of Fatigue.
(12) Y.S. Garud, Transactions of the ASME, Vol 103, (1981) pp 118-125

LIST OF FIGURES

Figure 1. Biaxial fatigue cycles (a) in-phase (proportional) and (b) 90^{o} out-of-phase (non-proportional)

Figure 2. (a) Schematic of a body under biaxial loading, (b) Detail of a small section on the surface of the body shown in (a); accordingly, for (i) pure tension $\Phi = 45^{o}$ and 135^{o}, (ii) pure torsion $\Phi = 0^{o}$ and 90^{o}, (iii) biaxial proportional Φ is fixed but dependent on relative magnitudes of $\Delta\epsilon$ and $\Delta\gamma$, and (iv) biaxial 90^{o} out-of-phase Φ continuously rotates in a cycle and the rate of change of Φ depends on a number of factors.

Figure 3. Resolved shear stresses for the twelve octohedral slip systems in fcc crystal during a fatigue cycle, (a) for pure tension, (b) for pure torsion, (c) for biaxial proportional cycle and (d) for biaxial non-proportional cycle. In figures (a)-(c), only one slip system enjoys the privilege of maximum resolved shear stress during the complete fatigue cycle, while in (d) many slip systems enjoy this privilege, mainly due to the rotating maximum shear planes, shown in figure 2. These calculations were done for a random orientation.

Figure 4. Fatigue specimen drawing; all units are in cm.

Figure 5. High resolution darkfield TEM iamges of the gamma prime precipitates. (a) heat treatment A and (b) heat treatment F.

Figure 6. SEM micrographs of typical grain boundaries. (a) heat treatment A and (b) heat treatment F.

Figure 7. Typical LCF hysterisis loops. (a) torsional fatigue, (b) axial loop and (c) torsional loop for in-phase biaxial

fatigue, (d) axial loop and (e) torsional loop for 90° out-of-phase biaxial fatigue.

Figure 8. Cumulative glide plots for (a) torsional fatigue, (b) axial stress and (c) torsional stress for in-phase biaxial fatigue, (d) axial stress and (e) torsional stress for 90° out-of-phase biaxial fatigue. Heat treatment A

Figure 9. Same as in figure 8, for heat treatment F

Figure 10. Optical micrographs of polished and etched specimens showing slip traces. The specimen axis is horizontal. (a) and (b) torsional, (c) and (d) biaxial in-phase, and (e) and (f) biaxial 90° out-of-phase for heat treatments A and F respectively. Note that the slip traces are parallel to the predicted maximum shear planes.

Figure 11. Macrophotographs showing crack morphology. (a), (c) and (e) are the photographs for torsional, biaxial in-phase and biaxial 90° out-of-phase tests and (b), (d) and (f) are corresponding shematic showing the crack orientation.

Figure 12. Typical example of optical photograph showing microcracks.

Figure 13. Typical example of SEM photograph showing striations on fracture surface.

LIST OF TABLES

LIST OF SYMBOLS

τ_{RSS} = Resolved shear stress on a slip plane,
ϕ_1, ϕ_2, ϕ_3 = Unit vector in the direction of the slip plane normal,
$\delta_1, \delta_2, \delta_3$ = Unit vector in the slip direction
$\sigma_{xx}, \sigma_{yy}, \sigma_{zz}$ = normal stresses at any point
$\tau_{xy}, \tau_{yz}, \tau_{zx}$ = shear stresses at any point
σ, τ = applied axial and shear stresses
Φ = angle between specimen axis and plane of maximum shear
ϵ, γ = applied axial and shear strains
ϕ = angle of twist in a torsional specimen
r_i, r_o, L = inner and outer radii and gage length of the specimen
T = applied torque on the specimen
$\Delta\epsilon_t, \Delta\epsilon_p$ = total and plastic axial strain ranges
$\Delta\gamma_t, \Delta\gamma_p$ = total and plastic torsional strain ranges
N_f = number of cycles to failure (using the 10%-drop-in-load criterion

Table I Composition of Waspaloy Plate (in Wt. Pct.)

C	Co	Cr	Mo	Al	Ti	Fe	Mn
.046	13.93	19.25	4.16	1.36	3.02	1.17	.03

Si	S	P	Cu	Sn	Pb	B	Zr
.05	.002	.006	.02	.0007	.0001	.0051	.067

N	Mg	Bi	Ni
.004	.0011	<.250 ppm	Balance

Table II Microstructural Analysis

	Heat treatment A	Heat treatment F
Solution Treatment	2 hrs. @ 1010°C Oil Quench	2 hrs. @ 1100°C Oil Quench
Aging Treatment	24 hrs. @ 875°C Oil Quench	6 hrs. @ 730°C Oil Quench
Grain Size	ASTM #7 Avg. dia = 32Ìm	ASTM #2 Avg. dia = 180Ìm
Gamma prime ppte. particles size	3000 & 900 A	50 - 100 A
Grain boundary carbides	Numerous, very dense distribution	Coarse grains are free of carbides; fine grains as in A
Matrix carbides	Large blocky carbides along rolling direction	Same as in A + fine spherical carbides

Table III Fatigue Data

Test No.	Control mode	$\phi\epsilon_t$ %	$\phi\epsilon_p$ %	$\phi\psi_t$ %	$\phi\psi_p$ %	σ_{max} MPa	σ_{min} MPa	τ_{max} MPa	τ_{min} MPa	N_f cycles
F04	Tor/tot	-	-	3.00	1.76	-	-	435	435	2,497
F06	Tor/pla	-	-	2.19	1.00	-	-	421	421	3,462
F07	Tor/pla	-	-	1.32	0.30	-	-	372	372	10,326
F09	Tor/pla	-	-	1.00	0.10	-	-	138	138	21,613
F01	InΔ/pla	1.74	1.00	1.59	1.00	717	772	228	228	1,520
F02	InΔ/pla	0.91	0.30	0.80	0.30	648	676	200	200	5,117
F03	InΔ/tot	0.50	.088	1.00	0.22	414	441	290	290	12,573
F11	InΔ/tot	0.60	.060	0.60	.074	572	600	207	214	11,423
F08	OoΔ/pla	0.98	0.30	1.09	0.30	752	779	386	393	2,439
F10	OoΔ/pla	1.88	1.00	1.98	1.00	993	1,034	538	559	520
F05	OoΔ/tot	0.50	.005	1.00	0.10	538	579	359	365	5,727
F12	OoΔ/tot	0.60	.023	0.60	.045	607	662	221	234	12,573
A03	Tor/tot	-	-	3.00	1.73	-	-	448	434	3,351
A01	Tor/pla	-	-	1.38	0.30	-	-	372	372	19,761
A08	Tor/pla	-	-	2.41	1.00	-	-	434	428	3,705
A09	InΔ/pla	1.03	0.30	0.87	0.30	676	724	207	241	7,311
A11	InΔ/pla	1.92	1.00	1.69	1.00	731	841	228	221	1,429
A10	InΔ/tot	0.50	.064	1.00	0.18	434	483	310	296	24,214
A12	InΔ/tot	0.60	.054	0.60	.063	545	607	207	207	33,350
A02	OoΔ/pla	1.10	0.30	1.20	0.30	786	821	386	400	2,620
A06	OoΔ/pla	2.00	1.00	1.69	1.00	1,014	1,048	503	524	429
A05	OoΔ/tot	0.50	.007	1.00	.090	503	579	345	352	11,029
A07	OoΔ/tot	0.60	.026	0.60	.046	600	669	221	228	24,218

Notes:

(i) Control modes: Tor = Torsion; InΔ = in-phase; OoΔ = 90° out-of-phase
tot = total strain range controlled
pla = plastic strain range controlled

(ii) $\phi\epsilon_t$ = total axial strain range;
$\phi\epsilon_p$ = axial plastic strain range (axial fatigue loop width);
$\phi\psi_t$ = total tosional strain range;
$\phi\psi_p$ = torsional plastic strain range (torsional fatigue loop width)
σ_{max} = maximum axial stress (tensile);
σ_{min} = minimum axial stress (compressive);
τ_{max} = maximum torsional stress;
τ_{min} = minimum torsional stress;
N_f = number of cycles to failure.

(iii) All of the above parameters are sampled at $N_f/2$.

(iv) Fatigue loop widths do not really indicate the plastic strain range for the 90° out-of-phase biaxial fatigue tests, since for these tests the elastic unloading during a cycle is incomplete or totally absent; those data are however included here for the sake of completeness.

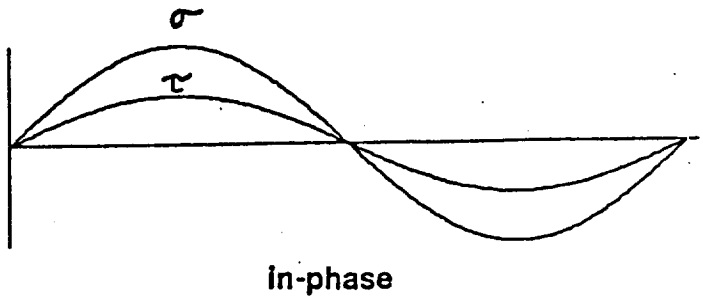

in-phase

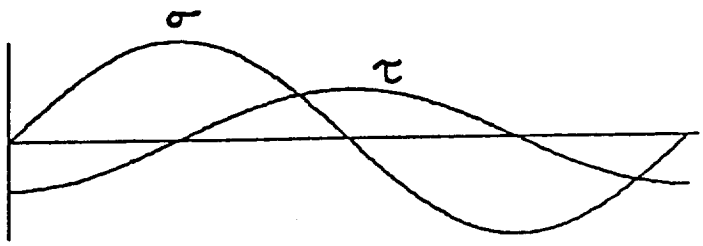

out-of-phase

Figure 1

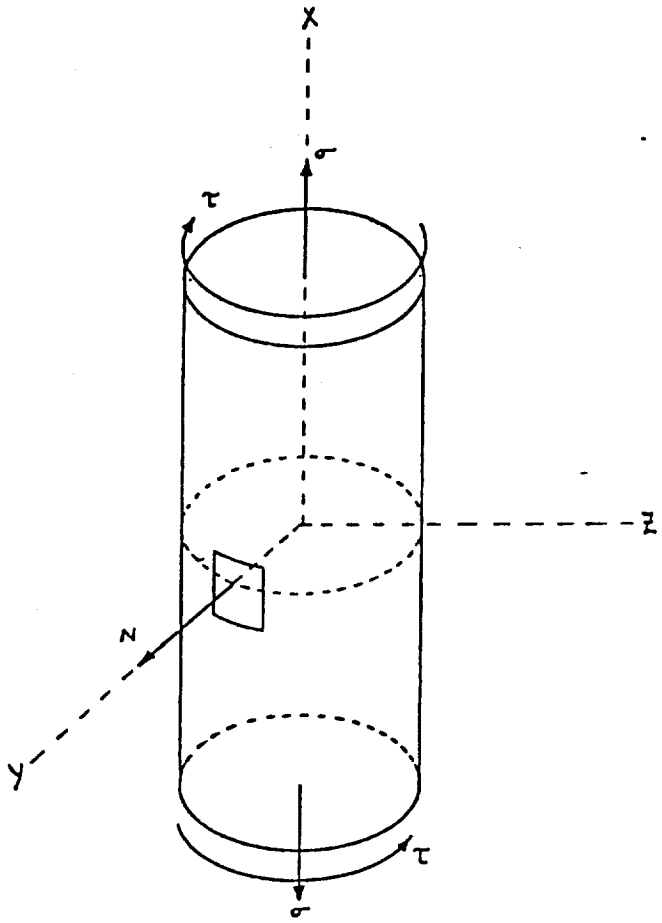

Figure 2(a)

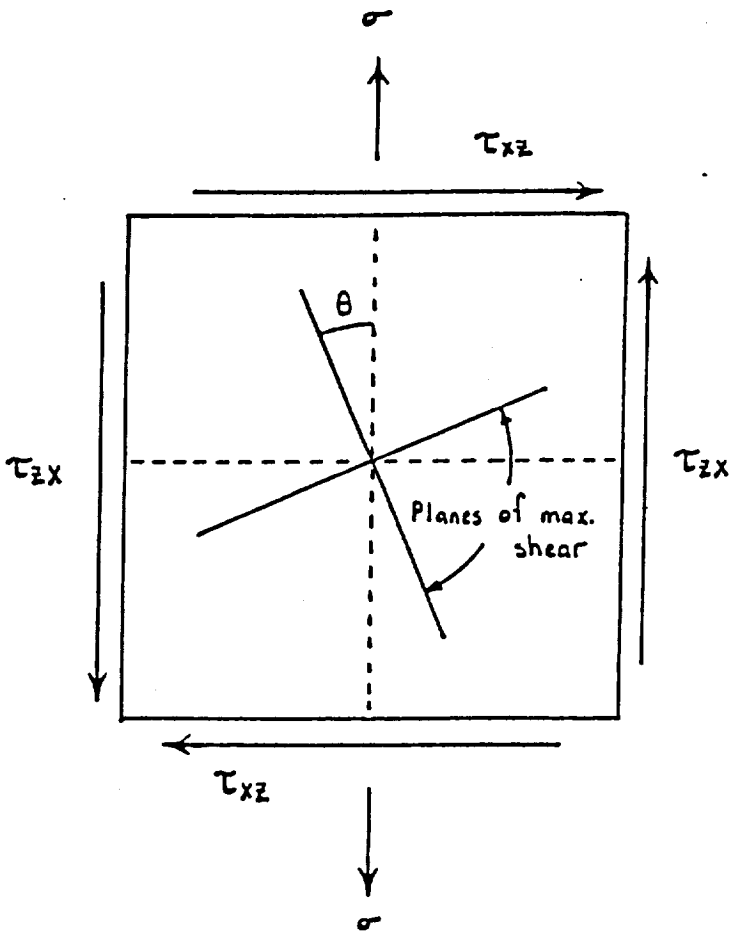

Figure 2(b)

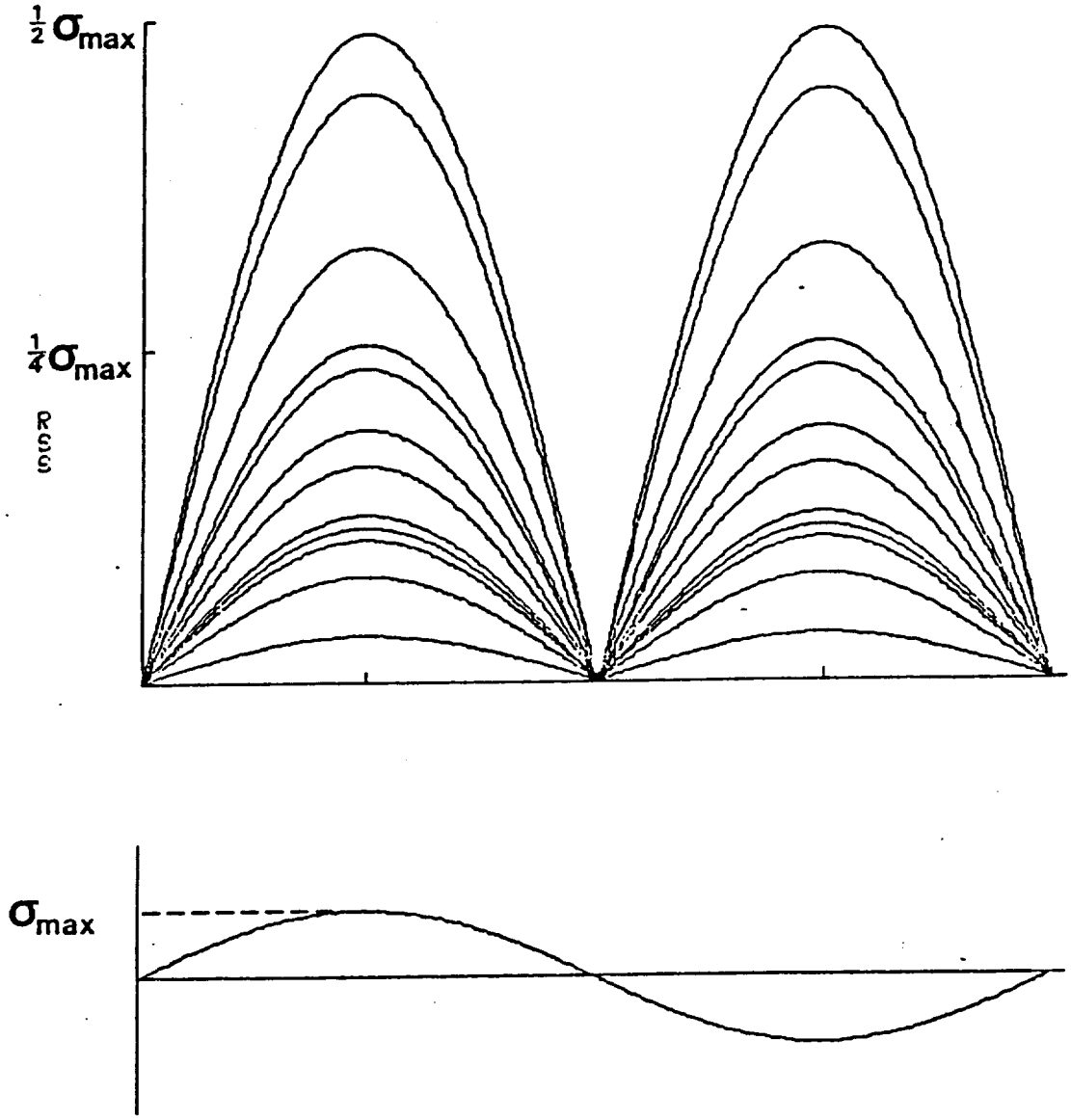

Figure 3(a)

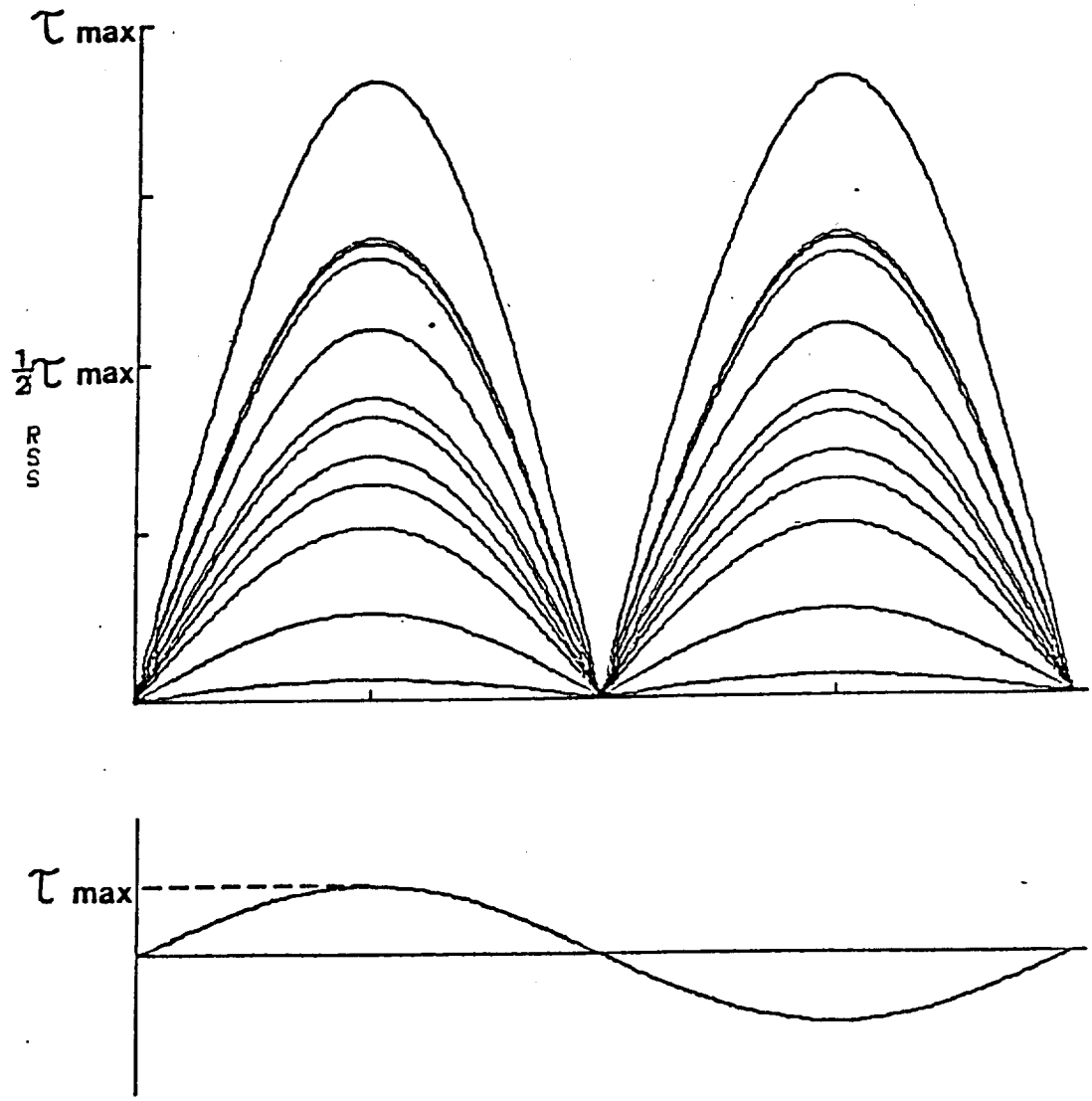

Figure 3(b)

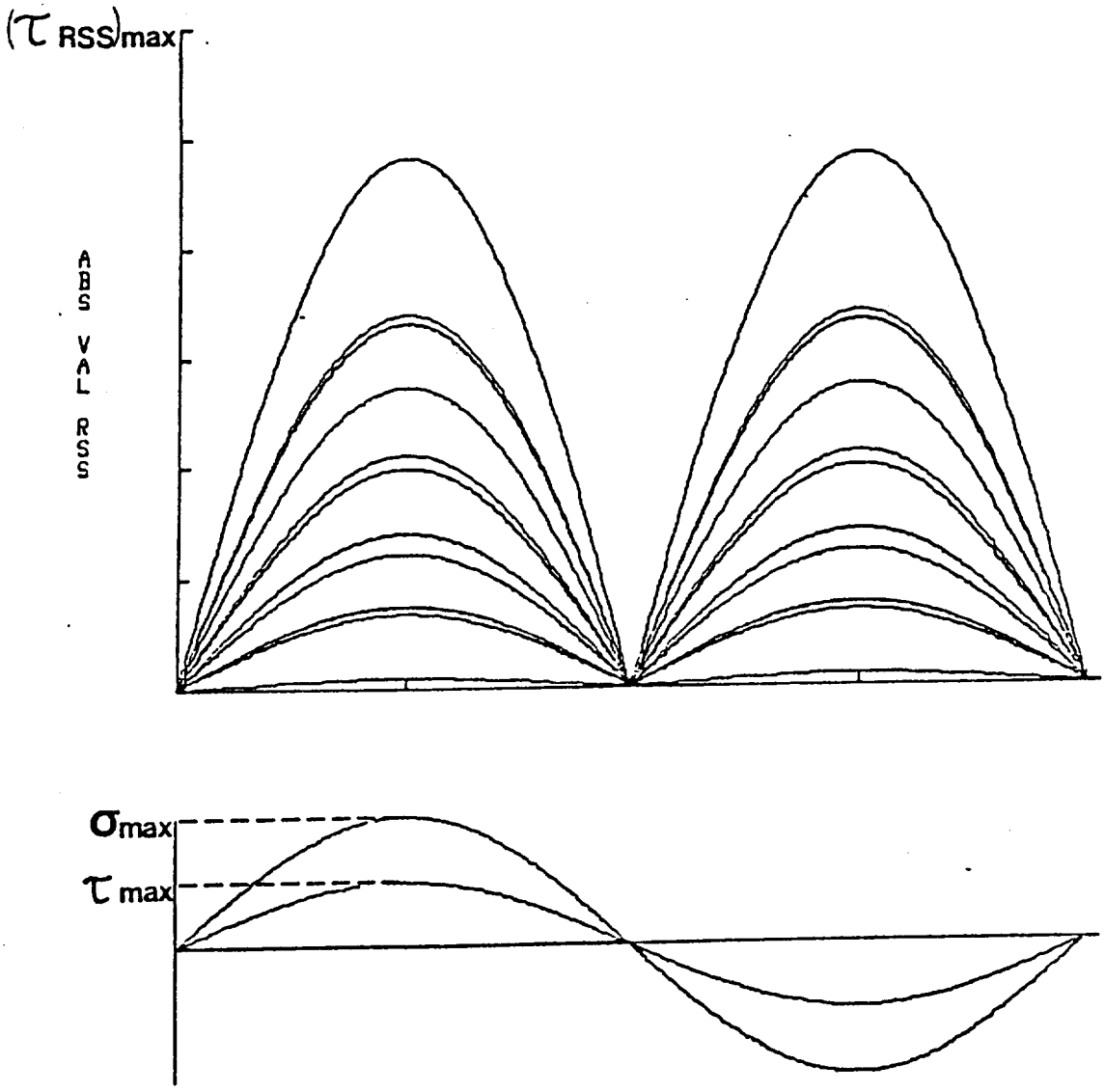

Figure 3(c)

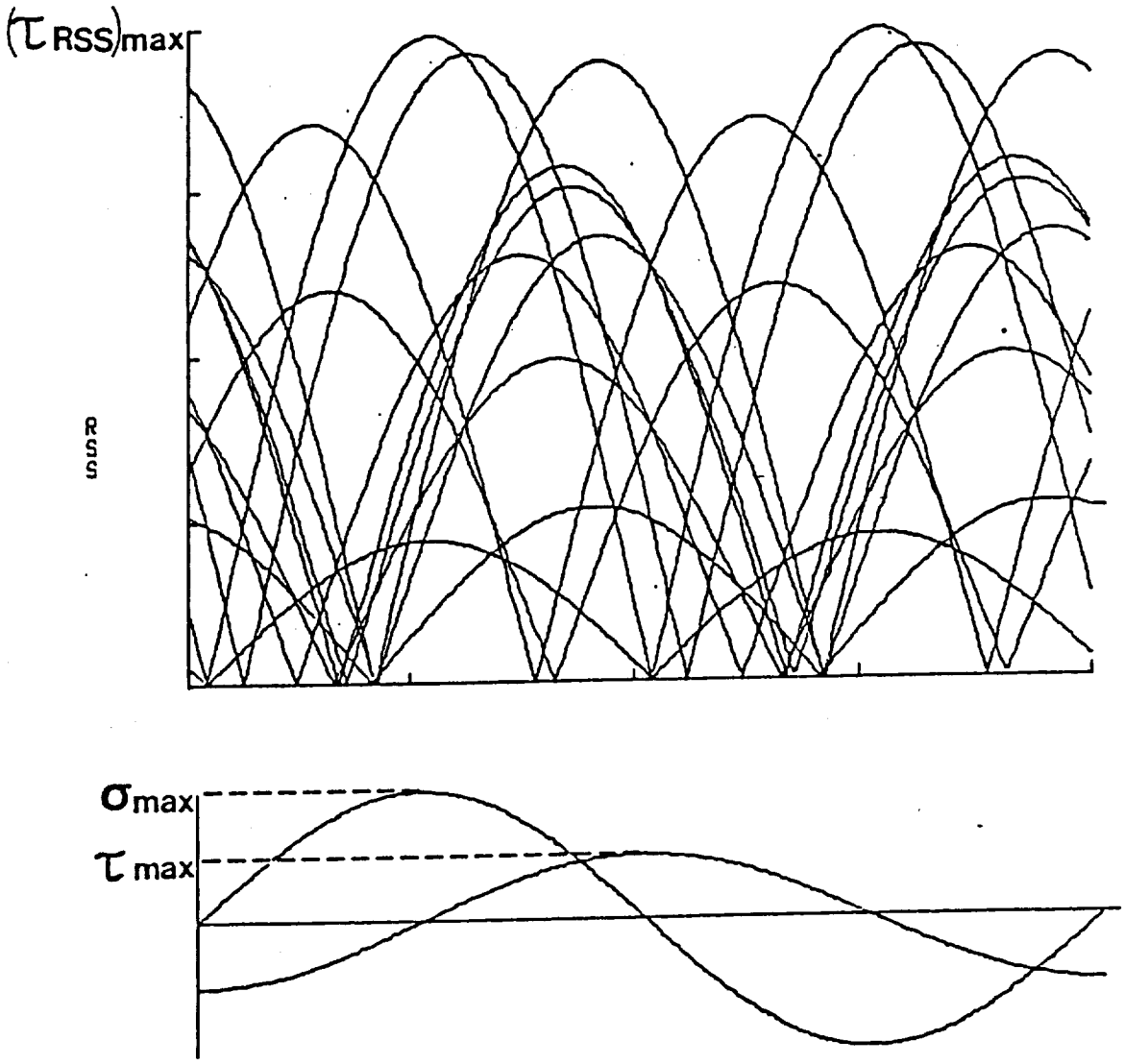

Figure 3(d)

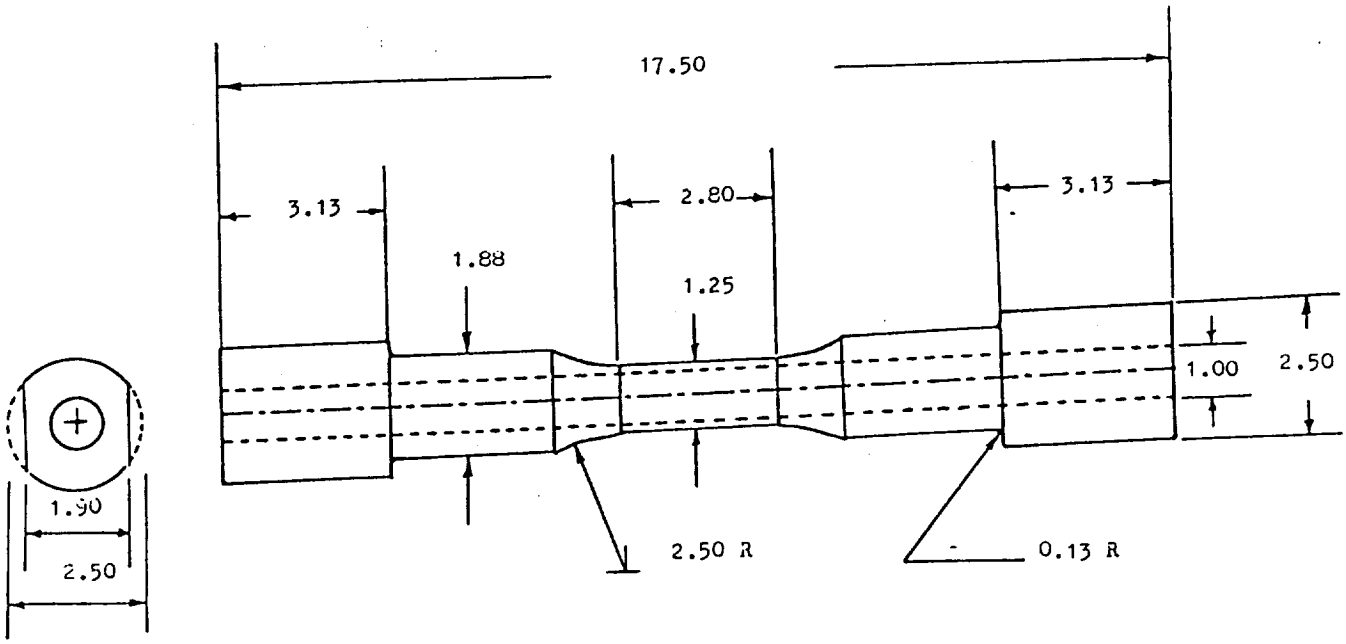

Figure 4

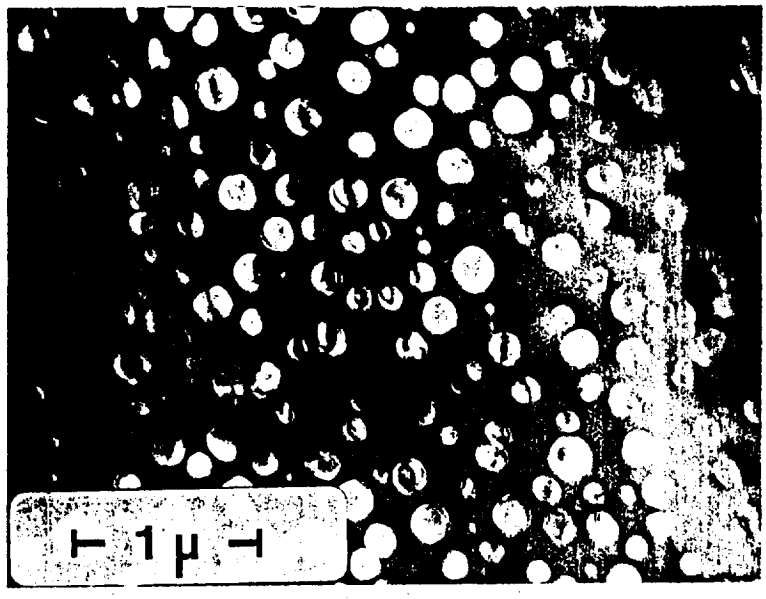

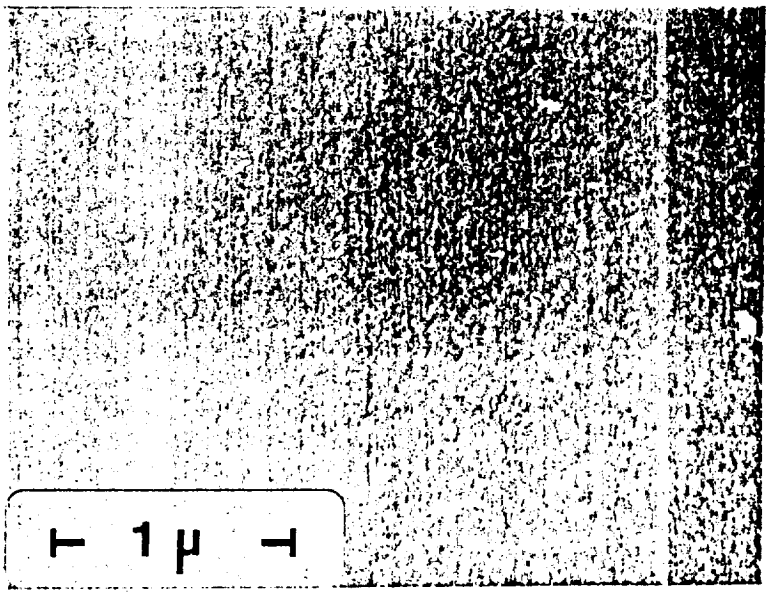

Figure 5

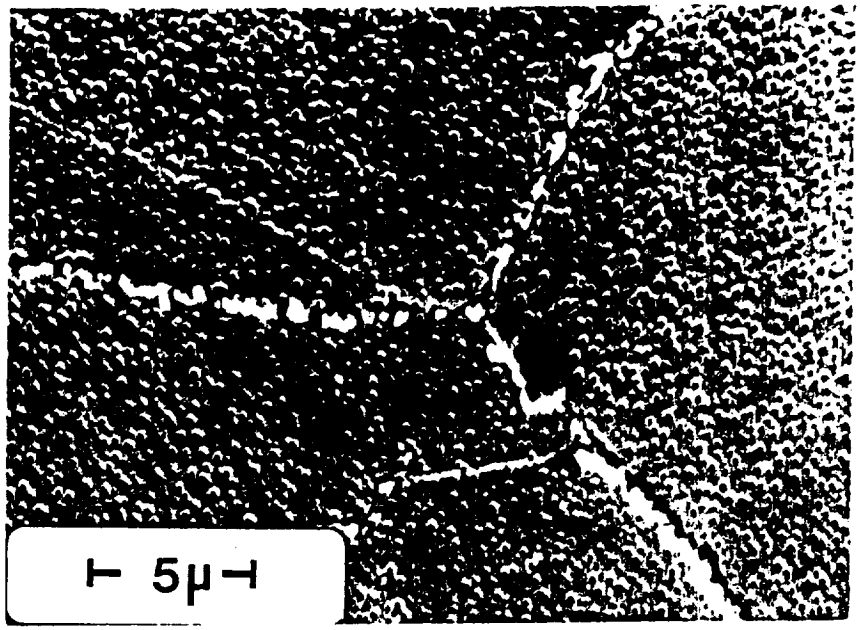

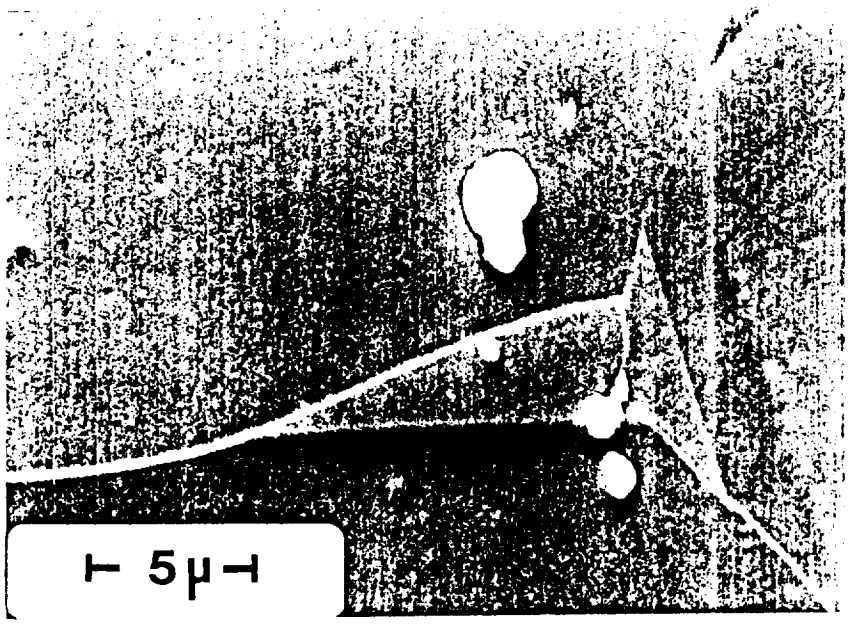

Figure 6

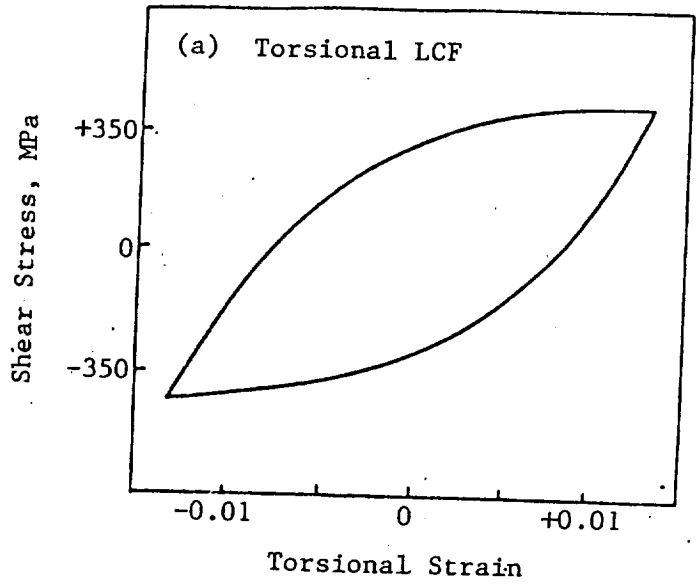
(a) Torsional LCF
Shear Stress, MPa
+350
0
-350
-0.01
0
+0.01
Torsional Strain

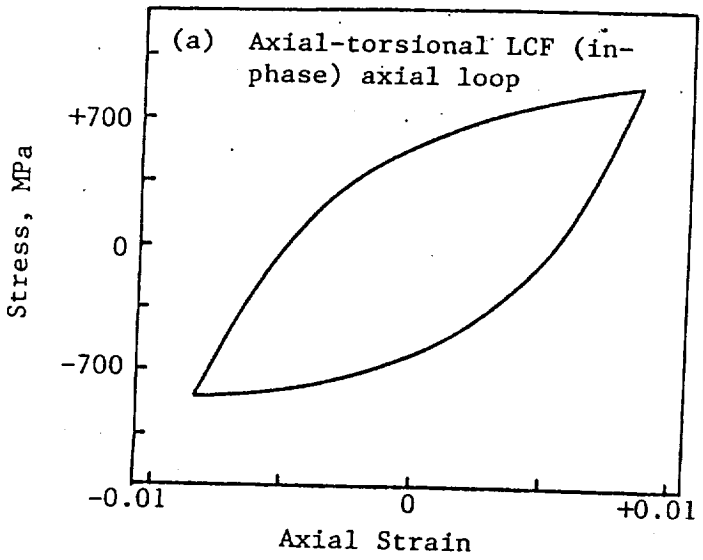
(a) Axial-torsional LCF (in-phase) axial loop
Stress, MPa
+700
0
-700
-0.01
0
+0.01
Axial Strain

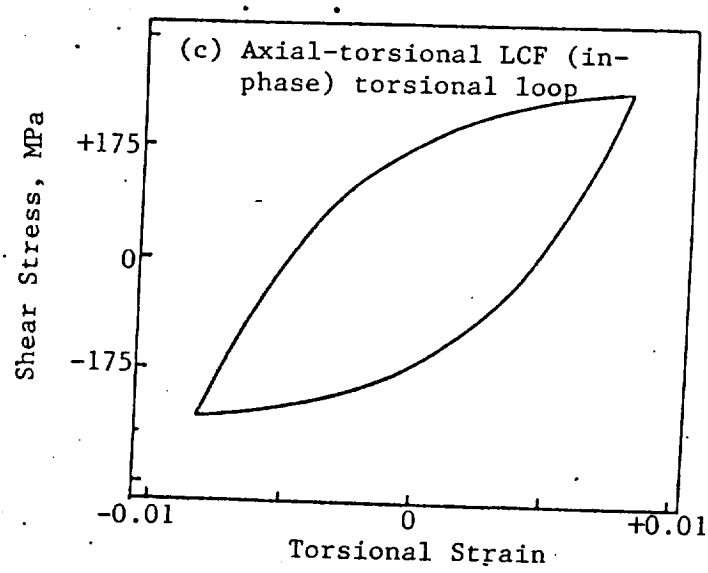
(c) Axial-torsional LCF (in-phase) torsional loop
Shear Stress, MPa
+175
0
-175
-0.01
0
+0.01
Torsional Strain

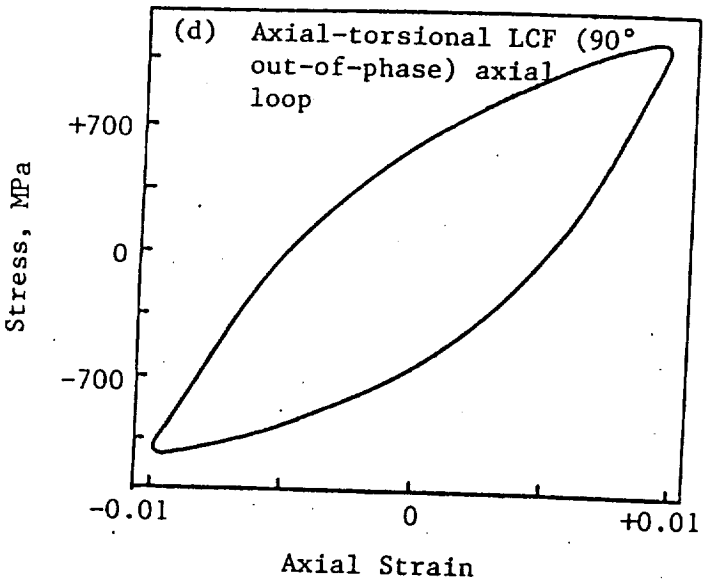
(d) Axial-torsional LCF (90° out-of-phase) axial loop
Stress, MPa
+700
0
-700
-0.01
0
+0.01
Axial Strain

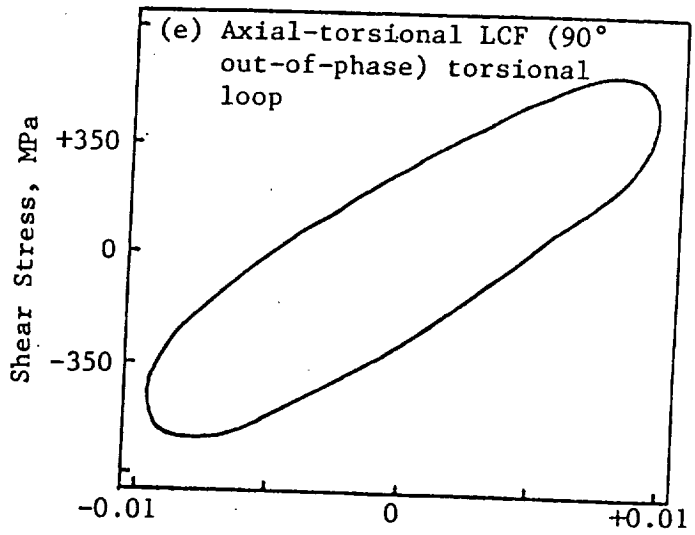
(e) Axial-torsional LCF (90° out-of-phase) torsional loop
Shear Stress, MPa
+350
0
-350
-0.01
0
+0.01
Torsional Strain

Figure 7

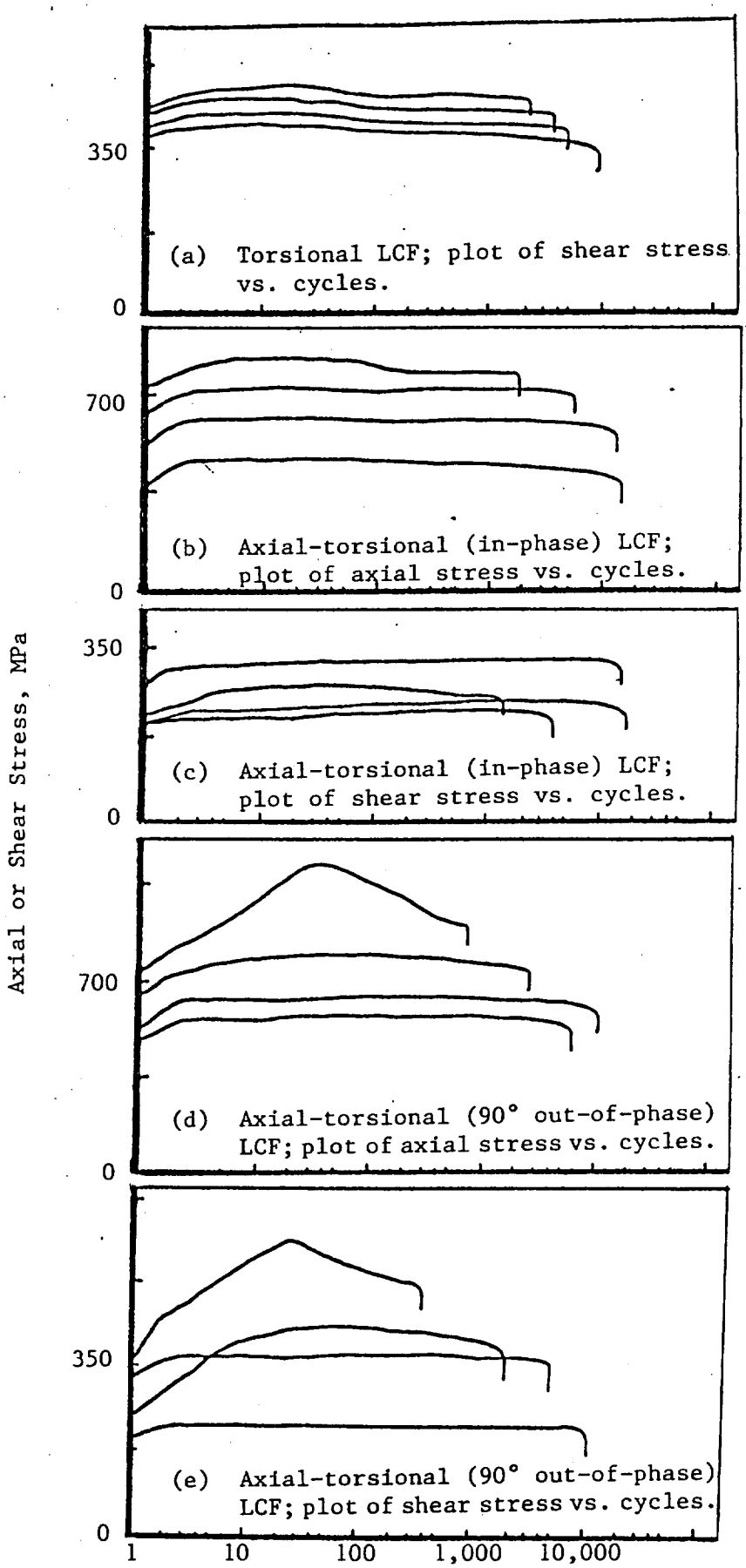
350
0
(a) Torsional LCF; plot of shear stress vs. cycles.
700
0
(b) Axial-torsional (in-phase) LCF; plot of axial stress vs. cycles.
350
0
(c) Axial-torsional (in-phase) LCF; plot of shear stress vs. cycles.
700
0
(d) Axial-torsional (90° out-of-phase) LCF; plot of axial stress vs. cycles.
350
0
(e) Axial-torsional (90° out-of-phase) LCF; plot of shear stress vs. cycles.
Axial or Shear Stress, MPa
1
10
100
1,000
10,000
Number of Cycles

Figure 8

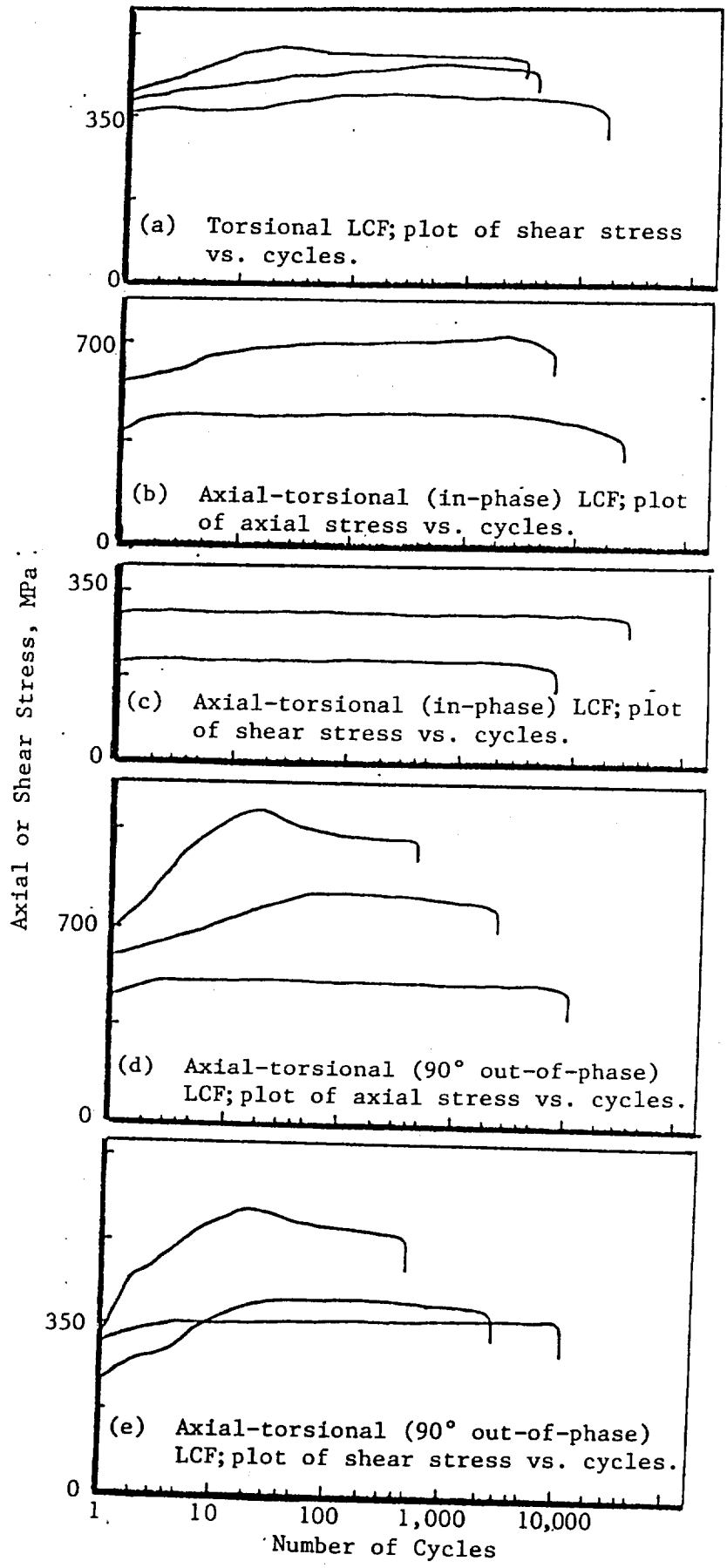
350
0
(a) Torsional LCF; plot of shear stress vs. cycles.
700
0
(b) Axial-torsional (in-phase) LCF; plot of axial stress vs. cycles.
350
0
(c) Axial-torsional (in-phase) LCF; plot of shear stress vs. cycles.
Axial or Shear Stress, MPa
700
0
(d) Axial-torsional (90° out-of-phase) LCF; plot of axial stress vs. cycles.
350
0
(e) Axial-torsional (90° out-of-phase) LCF; plot of shear stress vs. cycles.
1
10
100
1,000
10,000
Number of Cycles

Figure 9

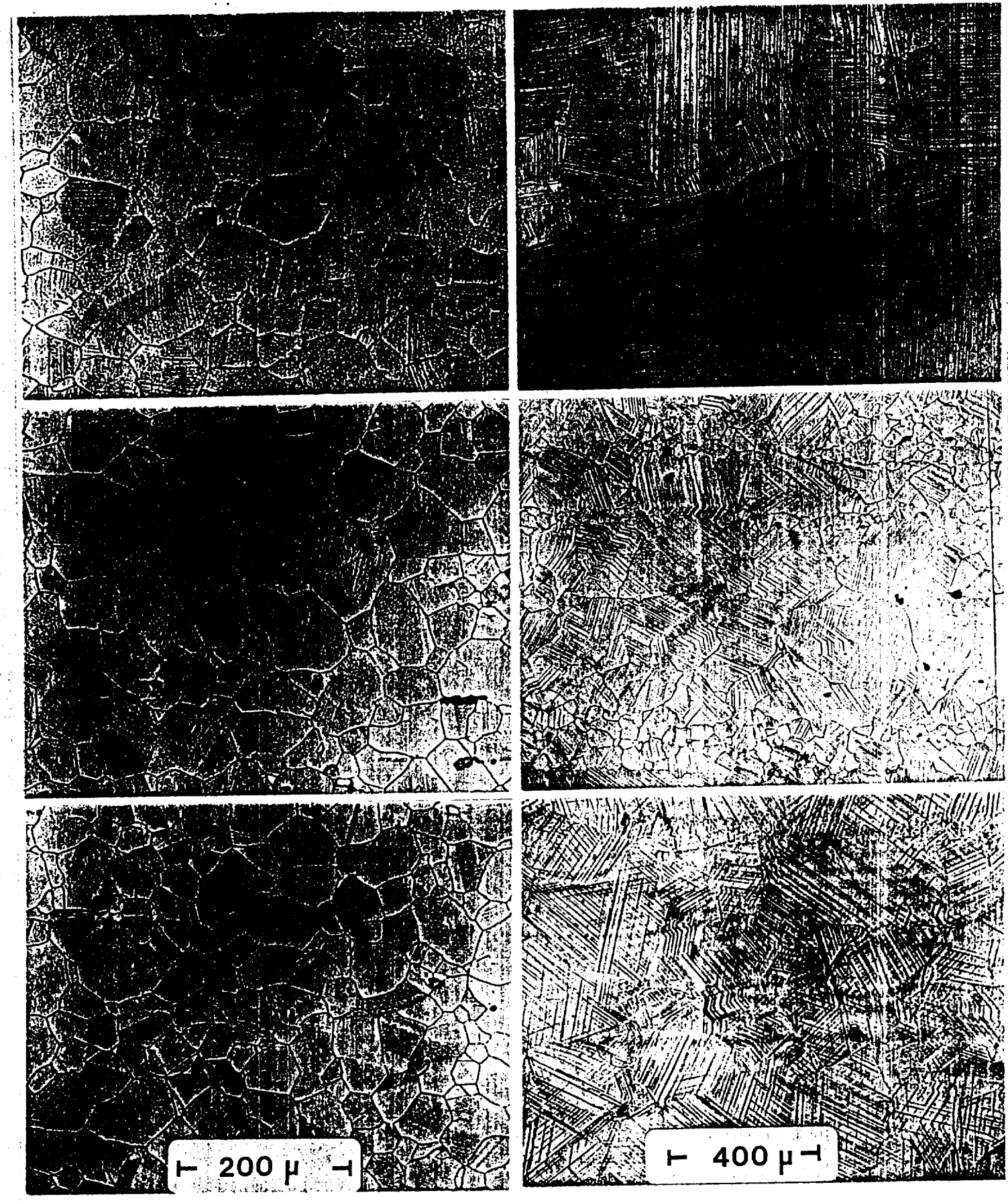

Figure 10

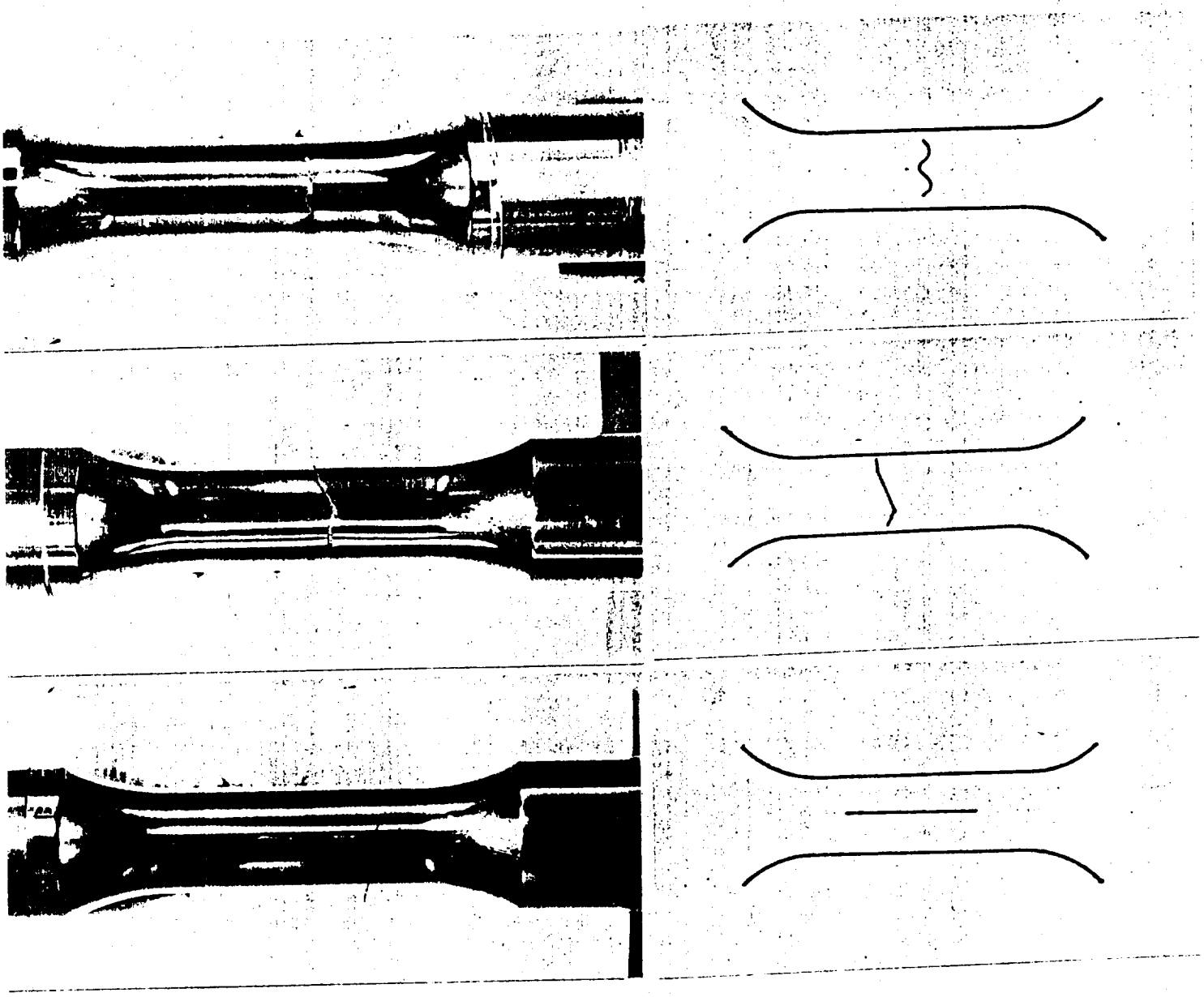

Figure 11

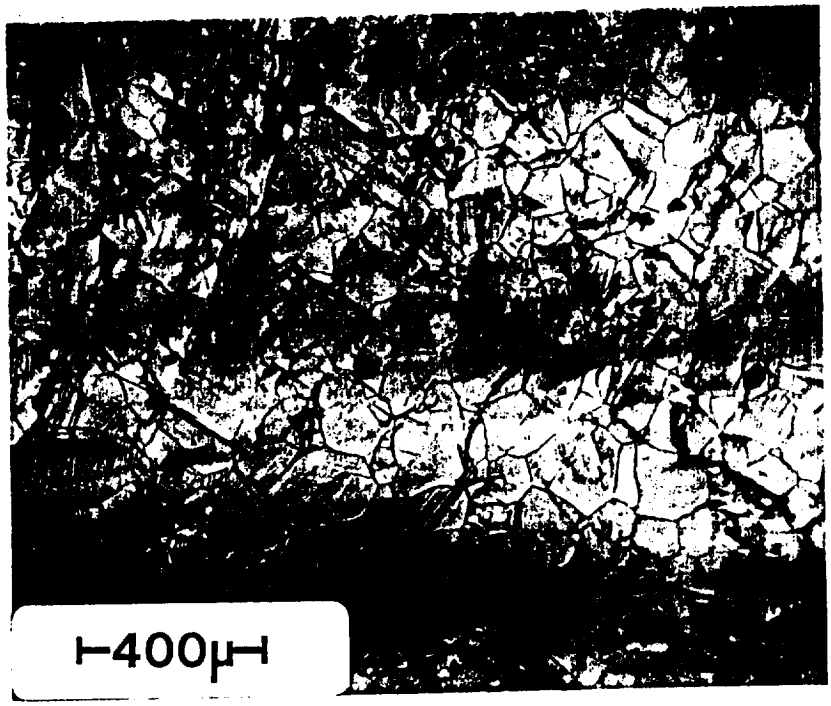

Figure 12

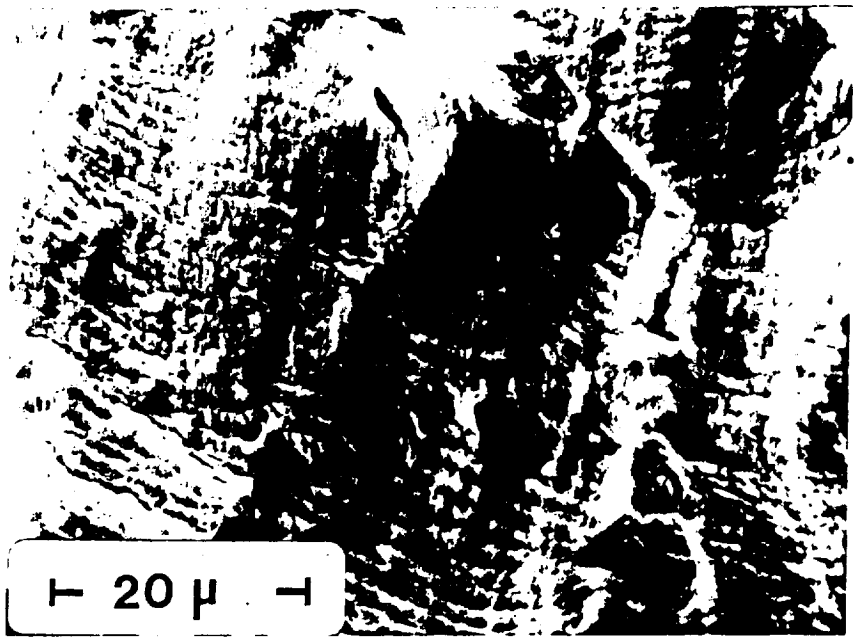

Figure 13

A life prediction method for tension-torsion fatigue:

ABSTRACT

A life prediction model has been developed using a cyclic equivalent strain approach for predicting biaxial (tension - torsion) fatigue lives based on uniaxial fatigue data. The cyclic equivalent strain approach has enabled us to combine uniaxial, torsional and biaxial (tension-torsion) fatigue data into a single life equation. The above model was applied successfully to experimental data available in Waspaloy (two heat treatments) and 1045 steel. A comparison with other life models has also been made.

1. INTRODUCTION

Many strucural members and machine components are subjected to repeated loading and therefore fatigue is one of the major considerations in their design. A number of life prediction methods are available for uniaxial cyclic loading (1). Actual structural elements, however, may often be subjected to multiaxial cyclic loading and a life prediction methodology common to these different loading conditions is essential for design applications. Once such a method becomes available, one can predict multiaxial fatigue life from uniaxial fatigue data. Most of the current multiaxial fatigue life prediction criteria (2) are limited to proportional loading conditions* and application of these criteria to non-proportional cyclic loading leads to significant error.

This paper describes a Coffin-Manson type fatigue life prediction methodology for complex biaxial loading conditions based on cyclic equivalent strain. Under proportional loading conditions, the cyclic equivalent strain is determined by using Von-Mises criterion and under non-proportional loading conditions a correction factor to the equivalent strain is introduced based on the strain path, which is phase angle dependent. Through this correction factor it is shown that one can normalize any type of loading into cyclic equivalent strain and the method is shown to apply effectively to experimental data available for Waspaloy and 1045 steel.

2. EQUIVALENT STRAIN APPROACH

Equivalent strain has been previously defined (3) for in-phase biaxial fatigue as:

---

*Note : Proportional loading refers to fatigue cycles in which the axial and torsional cycles are in-phase; non-proportional refers to conditions when they are not in-phase. The differnces are illustrated in figure 1.

$$\bar{\epsilon} = \frac{!2}{3} [(\epsilon_1-\epsilon_2)^2 + (\epsilon_2-\epsilon_3)^2 + (\epsilon_3-\epsilon_1)^2]^{\frac{1}{2}} \quad \ldots (1)$$

where ϵ_1, ϵ_2 and ϵ_3 are principal strains.
When condition of constancy of volume, i.e.,

$$\epsilon_1 + \epsilon_2 + \epsilon_3 = 0,$$

is invoked, equation (1) reduces to

$$\epsilon = (\frac{2}{3} [(\epsilon_1)^2 + (\epsilon_2)^2 + (\epsilon_3)^2])^{\frac{1}{2}} \quad \ldots (2)$$

When a thin walled tubular specimen is subjected to axial strain, e and torsional strain, c simultaneously, the applied strains are represented by the following strain tensor:

$$[\tilde{\epsilon}] = \begin{matrix} \epsilon & \frac{1}{2}\gamma & 0 \\ \frac{1}{2}\gamma & -\frac{1}{2}\epsilon & 0 \\ 0 & 0 & -\frac{1}{2}\epsilon \end{matrix} \quad \ldots (3)$$

The equivalent strain $\bar{\epsilon}$ is obtained by calculating the principal strains of ϵ, and then substituting these into equation (2)

$$\bar{\epsilon} = \{\epsilon^2 + (\gamma^2/3)\}^{\frac{1}{2}} \quad \ldots (4)$$

Strain states leading to similar ϵ values, regardless of the individual values torsional and axial strains, are expected to result in similar fatigue lives. Use of the above equivalent strain is justified only when the directions of the principal strains do not change during cyclic loading (4), i.e., under proportional loading conditions. For non-proportional cyclic loading, the principal axes rotate continuously and elastic unloading is normally incomplete.

The net effect of rotation of the principal axes and the elastic unloading behaviour for non-proportional cyclic loading is the increase in the strain path per cycle and the increase in the area under the ϵ - γ strain space. For example, as shown in figures 2a and b, the strain path per cycle for non-proportional loading is $!2\pi(\epsilon_a^2 + \gamma_a^2)^{\frac{1}{2}}$, while for proportional loading it is $4(\epsilon_a^2 + \gamma_a^2)^{\frac{1}{2}}$. Thus, the strain path for non-proportional loading is 11.1% greater than that for proportional loading.

The damage due to this increased strain path will depend on the amount of elastic unloading (or the lack of it), which in turn depends on the phase angle, ϕ , between the axial and the torsional strain. If one assumes that the area under the ϵ - γ space is indicative of the elastic unloading, i.e., the area is inversely proportional to elastic unloading, a correction factor, $f(\phi)$, for the cyclic equivalent strain given in equation (4) can

be developed. It is easily shown that the area under the $\epsilon - \gamma$ space is proportional to Sin ϕ.

Combining the increase in the strain path per cycle and the area under the $\epsilon - \gamma$ space, the correction factor becomes:

$$f(\phi) = 0.111 \text{ Sin } \phi \quad \ldots (5)$$

Now the generalized cyclic equivalent strain is given by:

$$\epsilon_{cycle} = \{1 + f(\phi)\} [\epsilon_a^2 + (\gamma_a^2)/3] \quad \ldots (6)$$

where $f(\phi)$, the correction factor takes a value of zero for proportional loading and a maximum value of 0.111 for 90^o out-of-phase, non-proportional loading. For intermediate phase angles, the correction factor falls between these two extreme values.

The underlying idea of this simple concept is that for a given set of axial and torsional strain ranges in a biaxial test, an increase in non-proportionality will result in considerably increased hardening and therefore it has the same effect as increasing the applied strains for a proportional biaxial test. For example, when in-phase and 90^o out-of phase biaxial fatigue tests were conducted under similar axial and torsional strain ranges, the out-of-phase loading was found to result in much higher stabilized stresses and shorter fatigue lives (5,6).

The generalized cyclic equivalent strain given in equation (6) can then be used in a Coffin-Manson type life relationship of the form:

$$N_f = A \, (\epsilon_{cycle})^b \quad \ldots (7)$$

3. VERIFICATION OF THE MODEL

The above life prediction method enables us to combine experimental data from uniaxial fatigue tests, torsional fatigue tests and proportional and non-proportional biaxial fatigue tests. In this section, the model is applied to experimental data from Waspaloy (two heat treatments) and 1045 steel.

3.1. Waspaloy

Lerch, Jayaraman and Antolovich (7) had conducted uniaxial fatigue tests on Waspaloy. In their study, Waspaloy was subjected to two heat treatments, referred to as A and F in reference (7), resulting in microstructures of small grain size (ASTM grain size 9) and coarse gamma prime precipitate particles (about 900 A in diameter) for heat treatment A and large grain size (ASTM grain size 3) and fine gamma prime precipitate particles (about 50-80 A in diameter) for heat treatment F. In a follow-up study, torsional and biaxial tension-torsion (in-phase and 90^o out-of-phase) fatigue tests for similar microstructural conditions were conducted by Ditmars and Jayaraman (5). The experimental results from these two studies were analyzed using

the cyclic equivalent strain approach given in equations (6) and (7), and the corresponding Coffin-Manson type plots are shown in figures 3(a) and (b). As seen in these two figures, the data from uniaxial and multiaxial fatigue tests can be represented in one life curve using the cyclic equivalent strain approach.

3.2. 1045 Steel

Fatigue test data were obtained from two sources. Appel and Jayaraman (6) conducted in-phase and 90^{o} out-of-phase tension-torsion tests on 1045 steel. Fash et al. (8) conducted uniaxial, torsional and biaxial in-phase fatigue tests on 1045 steel. Data from these two sources were analyzed using the cyclic equivalent strain approach and the resulting life plot is shown in figure 4. Again this figure shows that data from uniaxial and multiaxial fatigue tests can be represented on one life curve.

3.3. Life prediction

In another exercise, attempts were made to predict biaxial in-phase and out-of-phase fatigue lives using only the uniaxial fatigue data for Waspaloy and 1045 steel. Here the uniaxial data for Waspaloy from reference 7 and that for 1045 steel from reference 8 were used to get the constants A and b in equation (7). Using these constants, fatigue lives for biaxial conditions (both proportional and non-proportional) corresponding to the experimental data for Waspaloy from reference 5 and that for 1045 steel from references 6 and 8 were predicted. Figure 5 shows the plot of predicted life vs. actual life. As seen in this figure most of the predicted data fall within the factor of two limits.

4. COMPARISON WITH OTHER LIFE PREDICTION METHODS

Zamrick and Frishmuth (9) used a "total strain", e_T, defined as:

$$\epsilon_T = (\epsilon_1^2 + \epsilon_2^2 + \epsilon_3^2)^{\frac{1}{2}} \qquad \ldots (8)$$

for correlating life. For biaxial case e_T is calculated using the equation given below:

$$\epsilon_T = \{ [\tfrac{1}{2} ([\epsilon''_x \sin \omega t - \nu \epsilon''_x \sin \omega t]$$

$$+ \{(\epsilon''_x \sin \omega t + \nu \epsilon''_x \sin \omega t)^2 + (\gamma''_{xy} \sin (\omega t+\phi))\}^{\frac{1}{2}})]^2$$

$$+ [\tfrac{1}{2} ([\epsilon''_x \sin \omega t - \nu \epsilon''_x \sin \omega t]$$

$$- \{(\epsilon''_x \sin \omega t + \nu \epsilon''_x \sin \omega t)^2 + (\gamma''_{xy} \sin (\omega t+\phi))^2)^{\frac{1}{2}})]^2$$

$$+ [- \nu \epsilon''_x \sin \omega t]^2 \}^{\frac{1}{2}} \qquad \ldots (9)$$

where,

ϵ''_x, γ''_{xy} = maximum applied axial and torsional strains,

ω = frequency of straining,

ν = Poisson's ratio and

t = time

$(\epsilon_T)_{max}$ was computed numerically using the above equation for each set of experimental data. Figures 6a and b plot $(\epsilon_T)_{max}$ vs. log N_f for the fatigue data in Waspaloy in the two heat treatments A and F respectively. Figure 6c shows a similar plot for the fatigue data in 1045 steel. Data correlation in these three figures are good. If the non-proportional data are disregarded, most of the other data points lie within a factor of 2 on life. The theory is unfortunately non-conservative for out-of-phase tests. Also, one of the major drawbacks of this model is that the calculation of $(\epsilon_T)_{max}$ involves determining the maximum of the function described in equation 9 numerically and these calculations are even more complex for phase angles other than 0^o or 90^o.

Garud (10) used inelastic work (W_p) per cycle as a measure of damage. For a biaxial test, inelastic work is simply the sum of axial and torsional hysterisis loop areas. Figures 7a and b plot log W_p vs. log N_f for fatigue data in Waspaloy in its two heat treatments A and F respectively. Again as seen in these figures, the data correlation is not good since many of the data points are outside the factor of 2 on life. In addition, one major problem in using this method is that prediction of W_p without actually running an experiment is very difficult.

The method proposed by Socie and Shield (11) is representative of a class of theories that are concerned with forces acting on some specific plane, rather than global quantities, which the previous methods considered. The main problem with these theories is that they can only be applied to proportional data. Therefore, non-proportional data will not be considered in the evaluation of this method. Socie and Shield use the quantity

$$D = \hat{\gamma}_p + 1.5\,\hat{\epsilon}_{np} + 1.5\,\hat{\tau}_n/E \qquad \ldots (10)$$

as a measure of damage. Figures 8a and b plot D vs. log N_f for fatigue data from Waspaloy in the two heat treatments A and F respectively. As indicated earlier, the non-proportional data were not included and inspite of this, as seen in these figures, the data correlation is not very good.

5. SUMMARY

A fatigue life model using cyclic equivalent strain approach has been developed to predict fatigue lives under multiaxial fatigue conditions. This model has been shown to apply well to

experimental data from Waspaloy and 1045 steel. As a comparison, three earlier models were applied to the same data base and the deficiencies in unifying all fatigue data have been indicated.

ACKNOWLEDGEMENTS

The authors gratefully acknowledge the financial support of the NASA Lewis Research Center, National Aeronautics and Space Administration, under grant NSG 3 506.

REFERENCES

(1) H.O. Fuchs and R.I. Stephens, Metal Fatigue Engineering, Wiley-Interscience, 1980.

(2) Y.S. Garud, Journal of Testing and Evaluation, Vol.9, (1981) pp 165-178

(3) ASME Boiler and Pressure Vessel Code Section III Division 1, ASME, New York, (1986) pp 90-91

(4) W.A. Backofen, Deformation Processing, Addison-Wesley Co., (1972), pp 33-34

(5) M.M. Ditmars and N. Jayaraman, paper under review

(6) M. Appel, Senior project thesis, University of Cincinnati, 1986.

(7) B.A. Lerch, N. Jayaraman and S.D. Antolovich, Materials Science and Engineering, Vol. 66, (1984), pp 151-166.

(8) J.W. Fash, D.F. Socie and D.L. McDowell, Multiaxial Fatigue, ASTM STP<853, (1985), pp 497-513.

(9) S.Y. Zamrick and R.E. Frishmuth, Experimental Mechanics, Vol. 13, (1973), pp 204-208.

(10) Y.S. Garud, Transactions of the ASME, Vol.103, (1981), pp 118-125.

(11) D.F. Socie and T.W. Shield, Journal of Engineering Materials and Technology, Vol.106, (19), pp 227-232.

LIST OF FIGURES

Figure 1. Biaxial fatigue cycles (a) in-phase (proportional) and (b) 90^{o} out-of-phase (non-proportional).

Figure 2. $\epsilon - \gamma$ space for strain controlled multiaxial fatigue, (a) in-phase and (b) 90^{o} out-of-phase.

Figure 3. Unified fatigue life plots for Waspaloy, (a) heat treatment A and (b) heat treatment F.

Figure 4. Unified fatigue life plot for 1045 steel.

Figure 5. Plot of predicted life vs. actual life for torsional and biaxial fatigue; the predictions are based on constants obtained from uniaxial fatigue data using the cyclic equivalent strain approach. Data from two heat treatments of Waspaloy and 1045 steel are presented.

Figure 6. Fatigue life plots using Zamrick and Frishmuth method, (a) Waspaloy, heat treatment A, (b) Waspaloy, heat treatment F and (c) 1045 steel.

Figure 7. Fatigue life plots for Waspaloy using Garud method, (a) heat treatment A and (b) heat treatment F

Figure 8. Fatigue life plots for Waspaloy using Socie and Shield method, (a) heat treatment A and (b) heat treatment F

NOMENCLATURE

$\epsilon_1, \epsilon_2, \epsilon_3$ = pricipal strains
ϵ, γ = normal and shear strain

ϵ_a, γ_a = axial and torsional strain amplitudes

ϵ = von Mises' type equivalent strain when axial and torsional cycles are in-phase

ϵ_{cycle} = cyclic equivalent strain under all biaxial conditions

ϕ = phase angle between axial and torsional cycles

$f(\phi)$ = correction factor to e for phase angles v = 0^o; f(v) takes values between 0 for v = 0^o and 0.111 for v = 90^o

N_f = cycles to failure
A and b = constants in life equation
$\epsilon''_x, \gamma''_{xy}$ = maximum applied axial and torsional strains as defined in reference 9
ϵ_T = total strain as defined in reference 9
ω = frequency of straining
t = time
ν = Poisson's ratio
D = plastic damage parameter
ϵ_p = plastic axial strain amplitudes normal to maximum shear planes (reference 11)
γ_p = plastic shear strain amplitude on the maximum shear plane (reference 11)
σ_n = stress amplitude normal to maximum shear plane (reference 11)

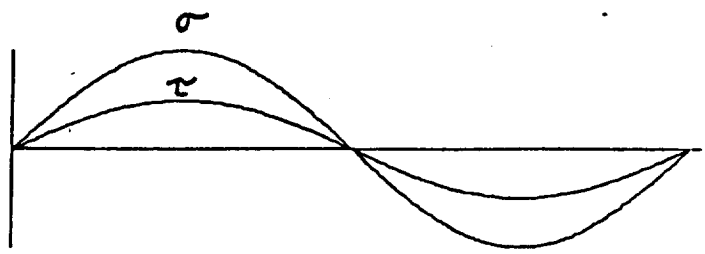

In-phase

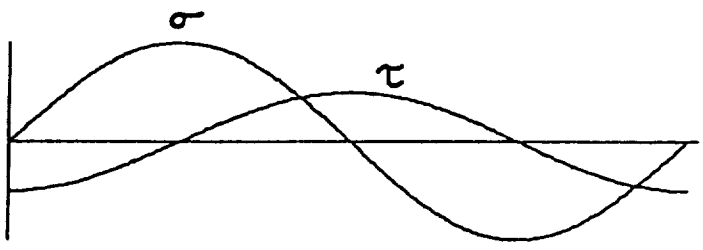

out-of-phase

Figure 1

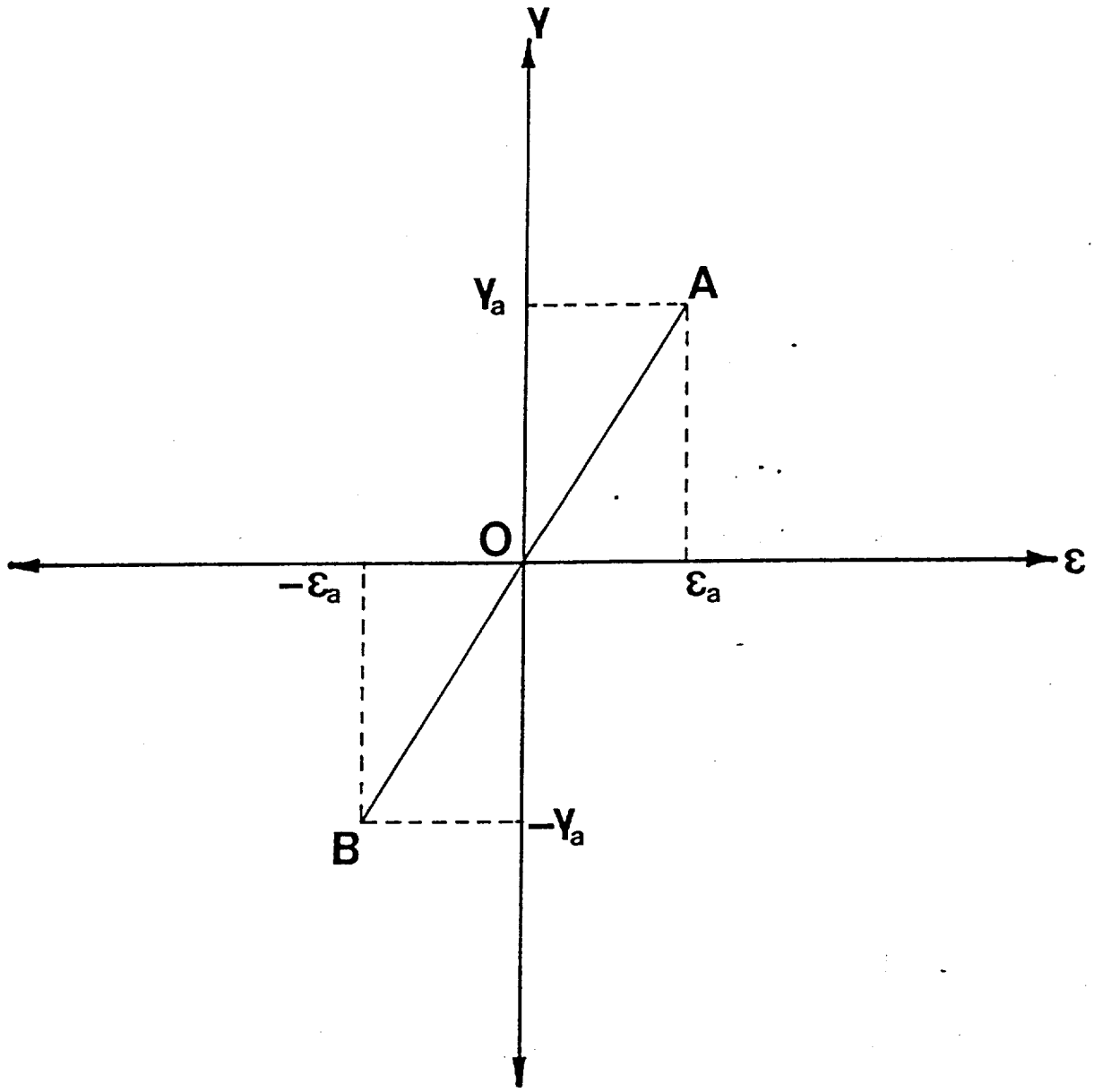

$$\text{Strain path per cycle} = 2\,\overline{AB}$$

$$= 4\sqrt{\varepsilon_a^2 + Y_a^2}$$

Figure 2(a)

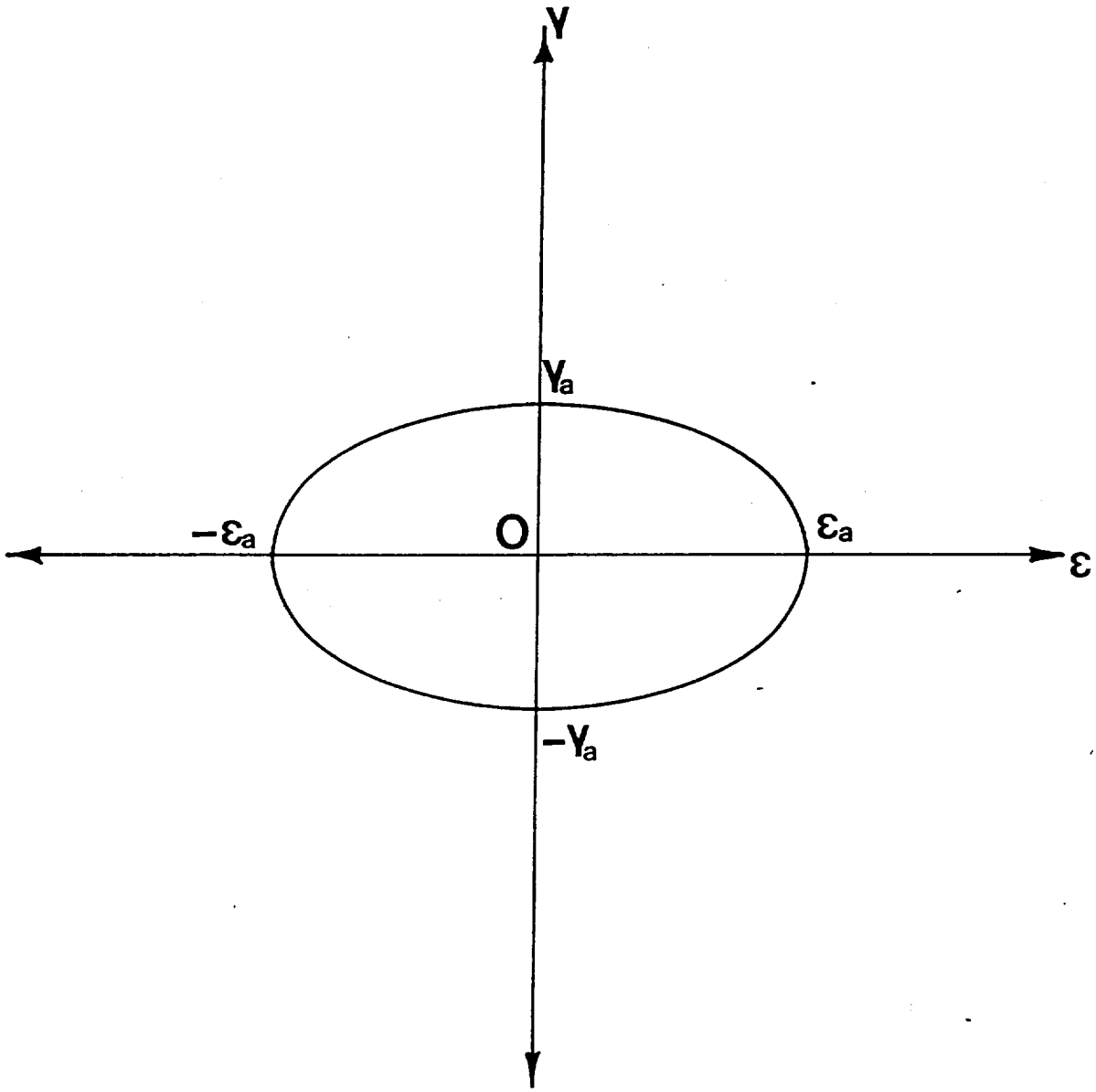

Strain path per cycle = perimeter of ellipse

$$= \sqrt{2}\,\Pi \sqrt{\varepsilon_a^2 + \gamma_a^2}$$

Figure 2(b)

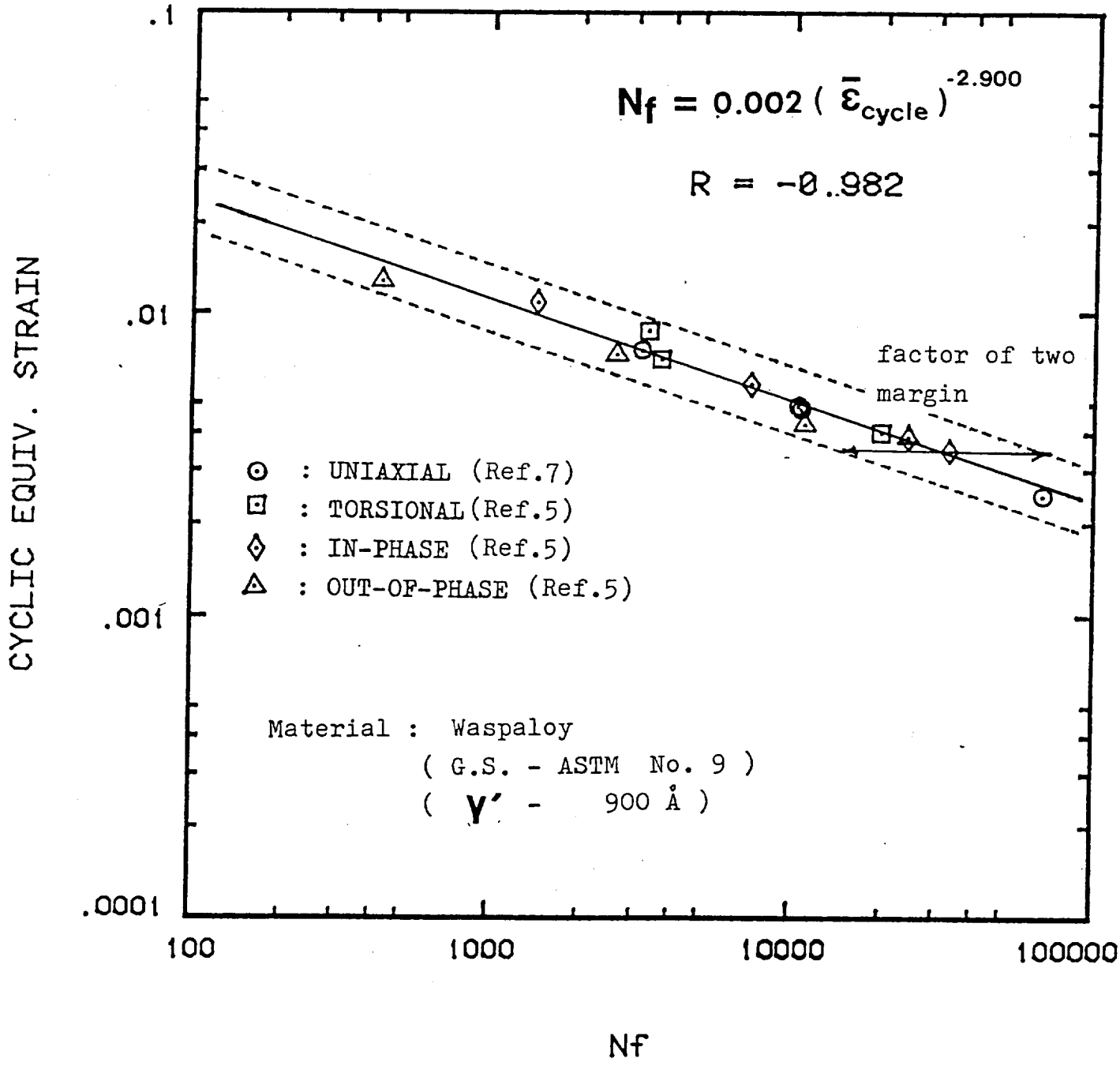
.1
.01
.001
.0001
100
1000
10000
100000
CYCLIC EQUIV. STRAIN
Nf
$N_f = 0.002 (\bar{\varepsilon}_{cycle})^{-2.900}$
R = -0.982
factor of two
margin
⊙ : UNIAXIAL (Ref.7)
⊡ : TORSIONAL (Ref.5)
◇ : IN-PHASE (Ref.5)
△ : OUT-OF-PHASE (Ref.5)
Material : Waspaloy
(G.S. - ASTM No. 9)
(γ' - 900 Å)

Figure 3(a)

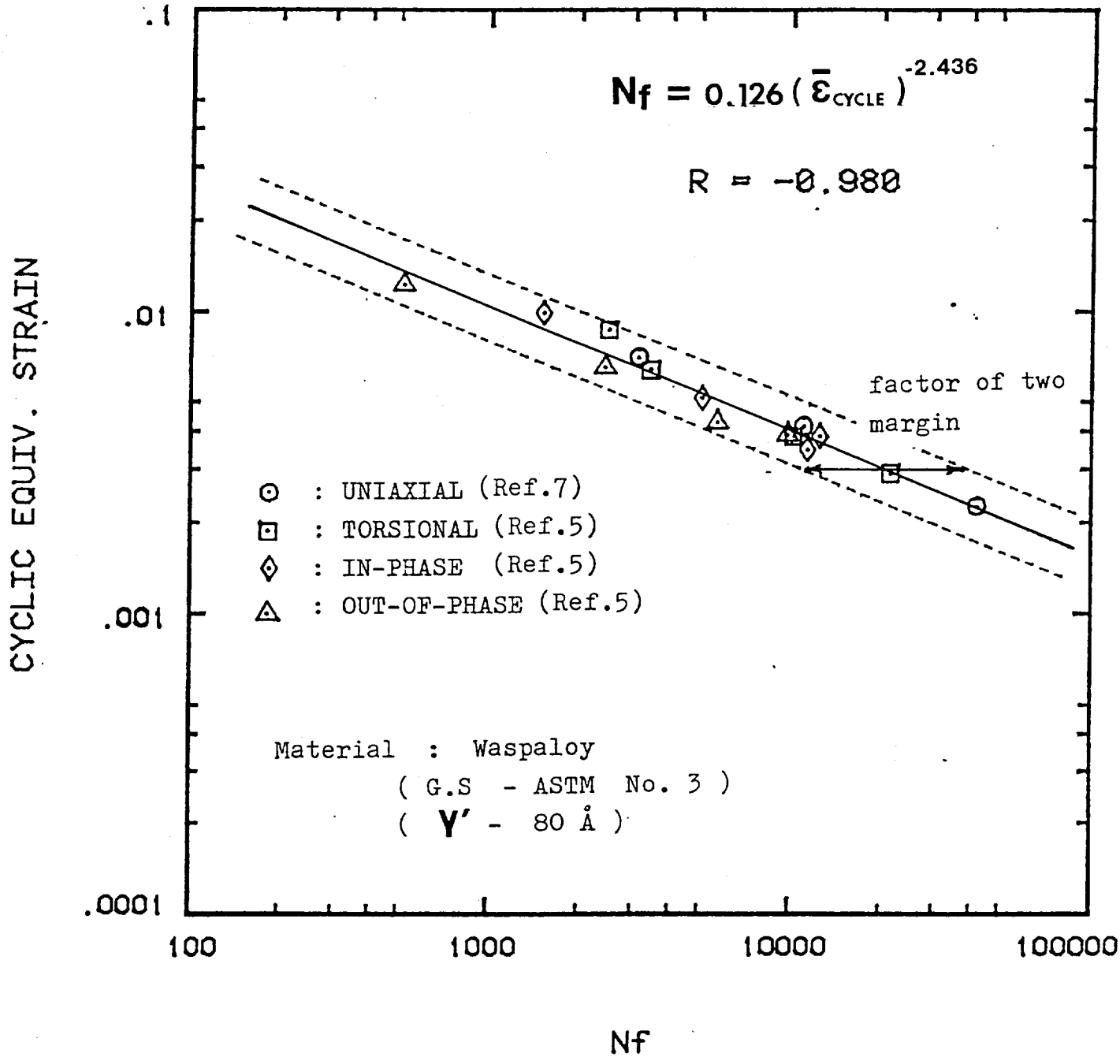
.1
.01
.001
.0001
CYCLIC EQUIV. STRAIN
$N_f = 0.126 (\bar{\varepsilon}_{CYCLE})^{-2.436}$
R = -0.980
factor of two
margin
⊙ : UNIAXIAL (Ref.7)
⊡ : TORSIONAL (Ref.5)
◇ : IN-PHASE (Ref.5)
△ : OUT-OF-PHASE (Ref.5)
Material : Waspaloy
(G.S - ASTM No. 3)
(γ' - 80 Å)
100
1000
10000
100000
Nf

Figure .3(b)

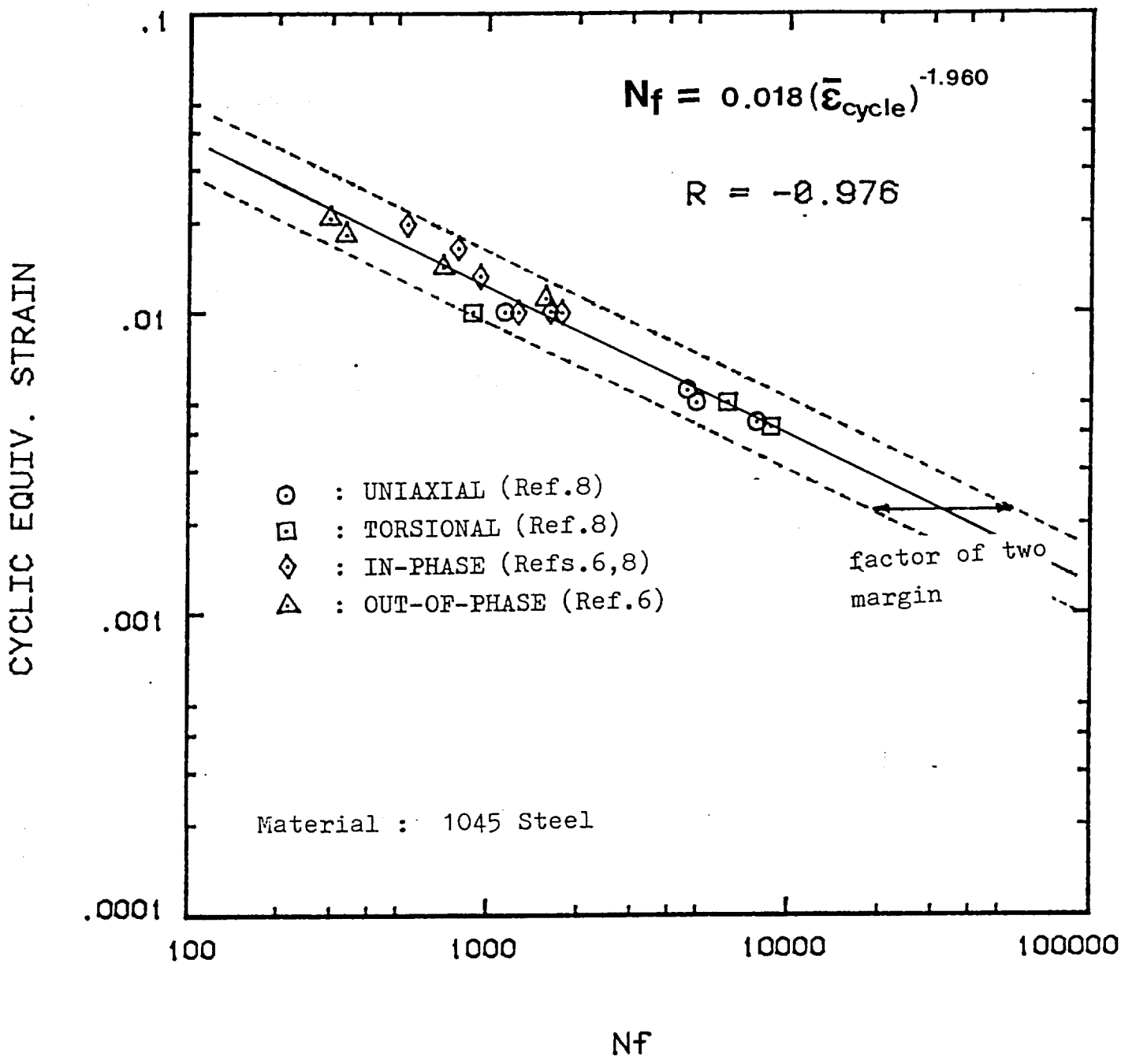
$N_f = 0.018(\bar{\varepsilon}_{cycle})^{-1.960}$
R = -0.976
CYCLIC EQUIV. STRAIN
.1
.01
.001
.0001
100
1000
10000
100000
Nf
⊙ : UNIAXIAL (Ref.8)
⊡ : TORSIONAL (Ref.8)
◇ : IN-PHASE (Refs.6,8)
△ : OUT-OF-PHASE (Ref.6)
factor of two margin
Material : 1045 Steel

Figure 4.

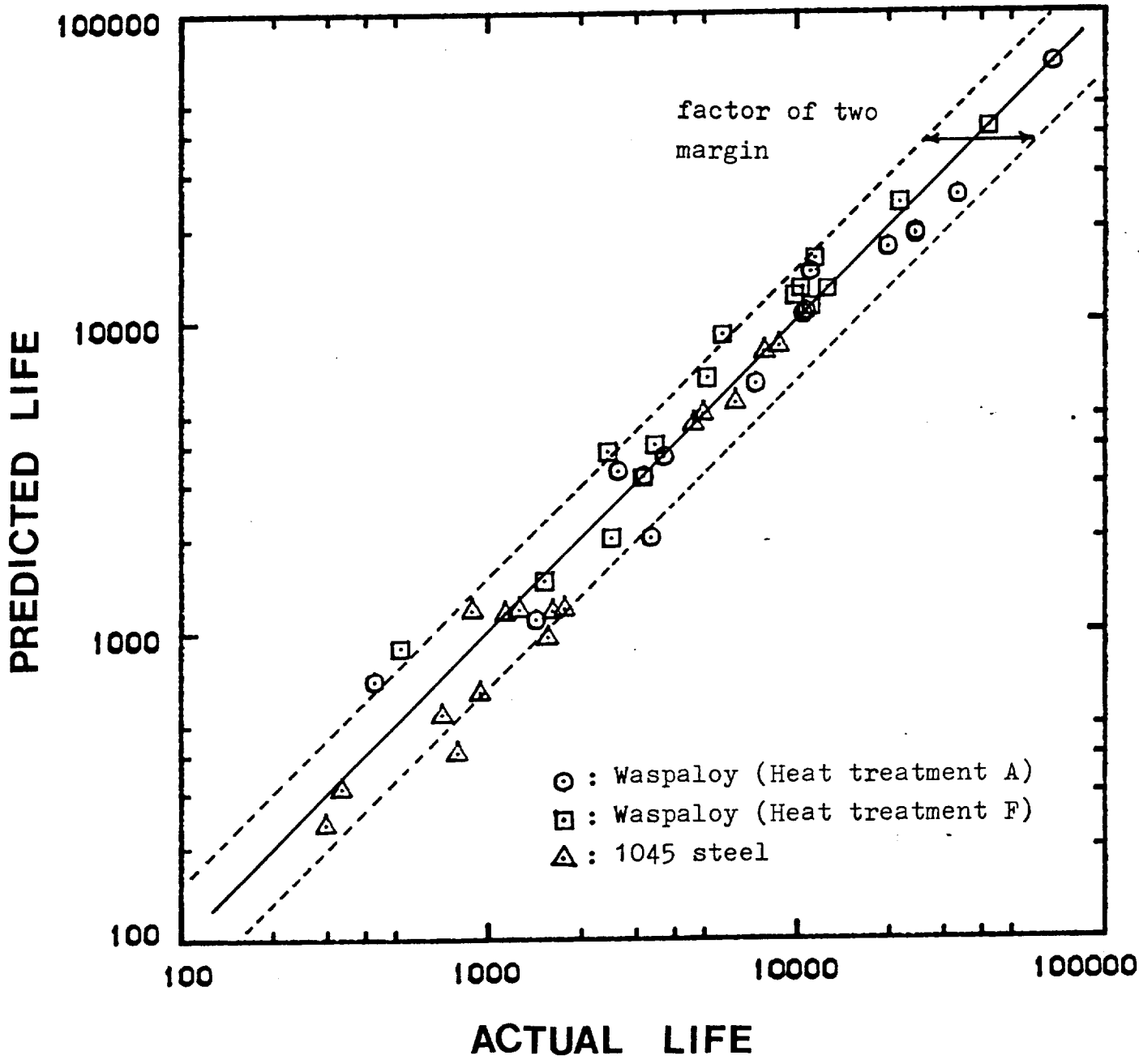
100000
10000
1000
100
PREDICTED LIFE
100
1000
10000
100000
ACTUAL LIFE
factor of two
margin
⊙ : Waspaloy (Heat treatment A)
⊡ : Waspaloy (Heat treatment F)
△ : 1045 steel

Figure 5.

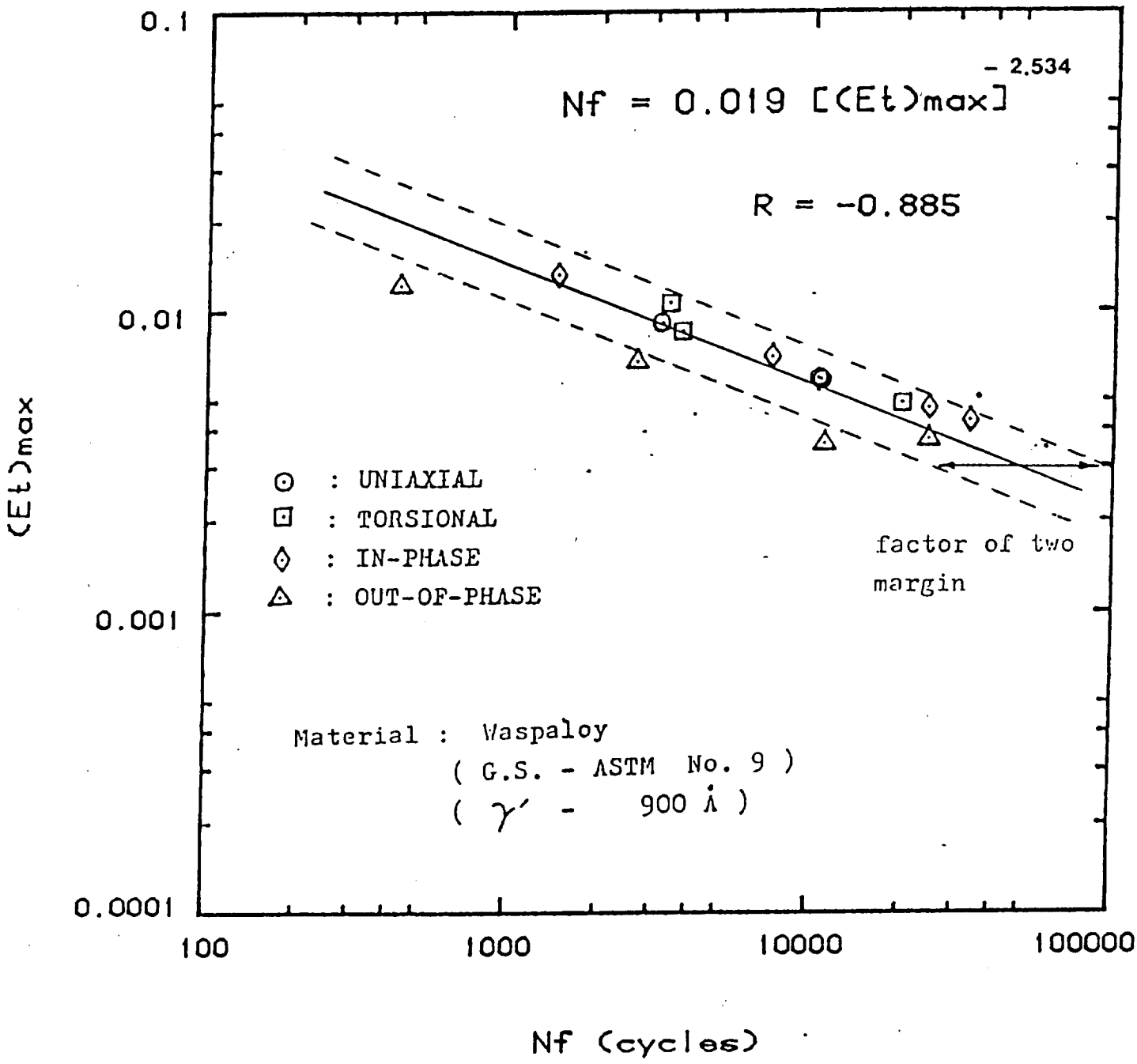
0.1
0.01
0.001
0.0001
100
1000
10000
100000
(Et)max
Nf (cycles)
Nf = 0.019 [(Et)max]^-2.534
R = -0.885
⊙ : UNIAXIAL
⊡ : TORSIONAL
◇ : IN-PHASE
△ : OUT-OF-PHASE
factor of two margin
Material : Waspaloy
(G.S. - ASTM No. 9)
(γ′ - 900 Å)

Figure 6(a)

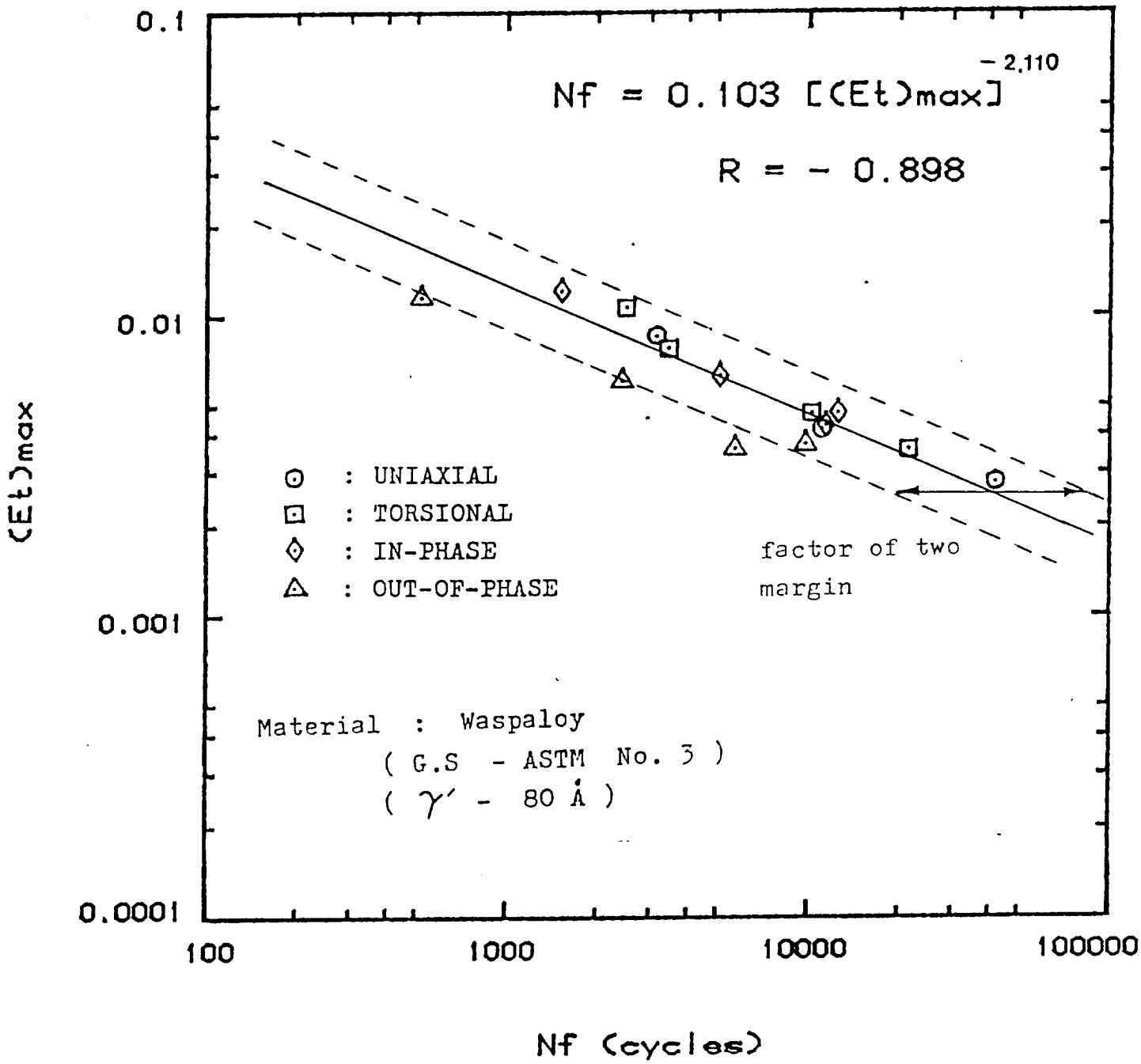
0.1
0.01
0.001
0.0001
100
1000
10000
100000
(Et)max
Nf (cycles)
Nf = 0.103 [(Et)max]^-2.110
R = - 0.898
⊙ : UNIAXIAL
⊡ : TORSIONAL
◇ : IN-PHASE
△ : OUT-OF-PHASE
factor of two
margin
Material : Waspaloy
(G.S - ASTM No. 3)
(γ′ - 80 Å)

Figure 6(b)

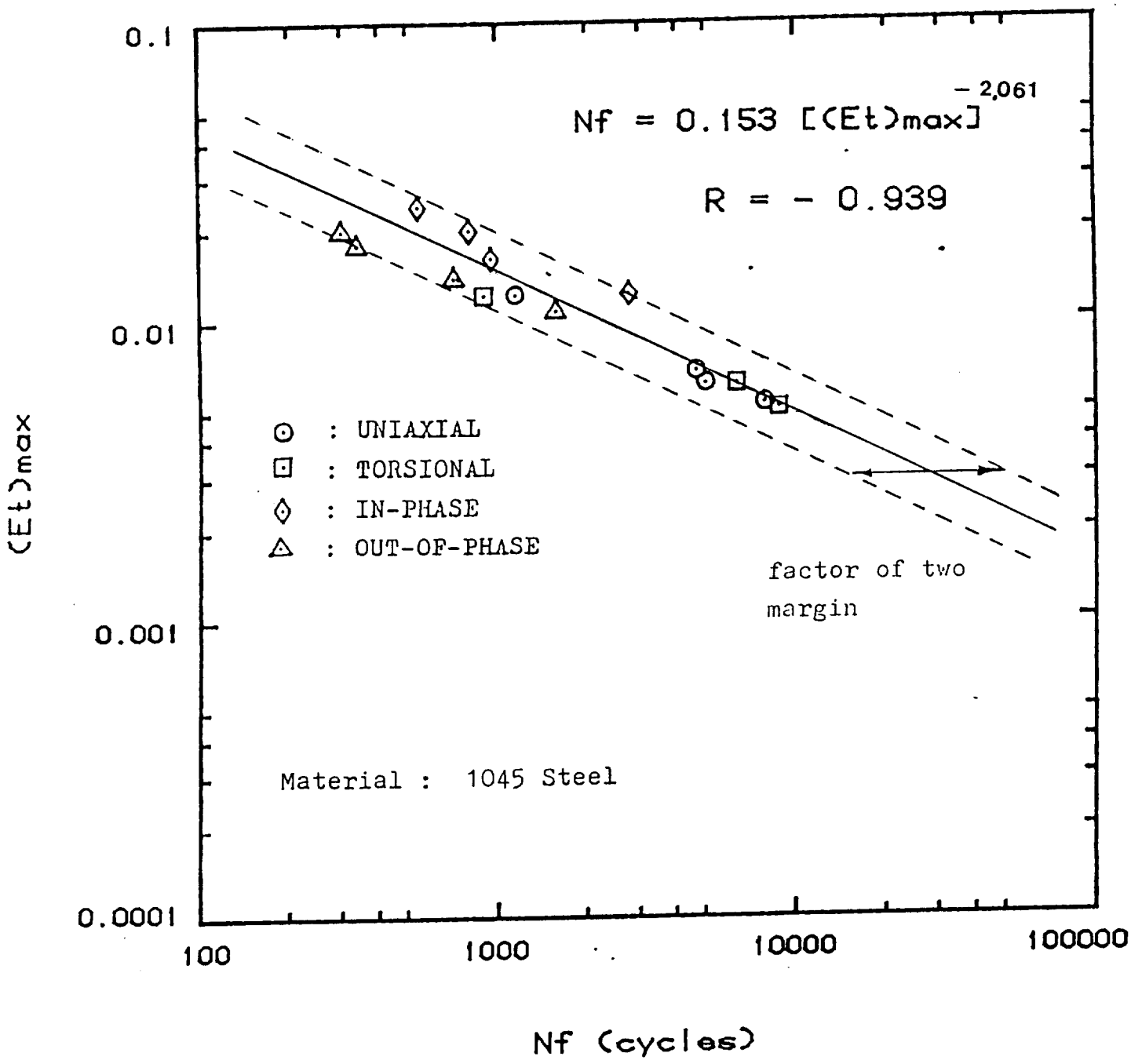
0.1
0.01
0.001
0.0001
100
1000
10000
100000
(Et)max
Nf (cycles)
Nf = 0.153 [(Et)max]^-2.061
R = - 0.939
⊙ : UNIAXIAL
⊡ : TORSIONAL
◇ : IN-PHASE
△ : OUT-OF-PHASE
factor of two
margin
Material : 1045 Steel

Figure 6 (c)

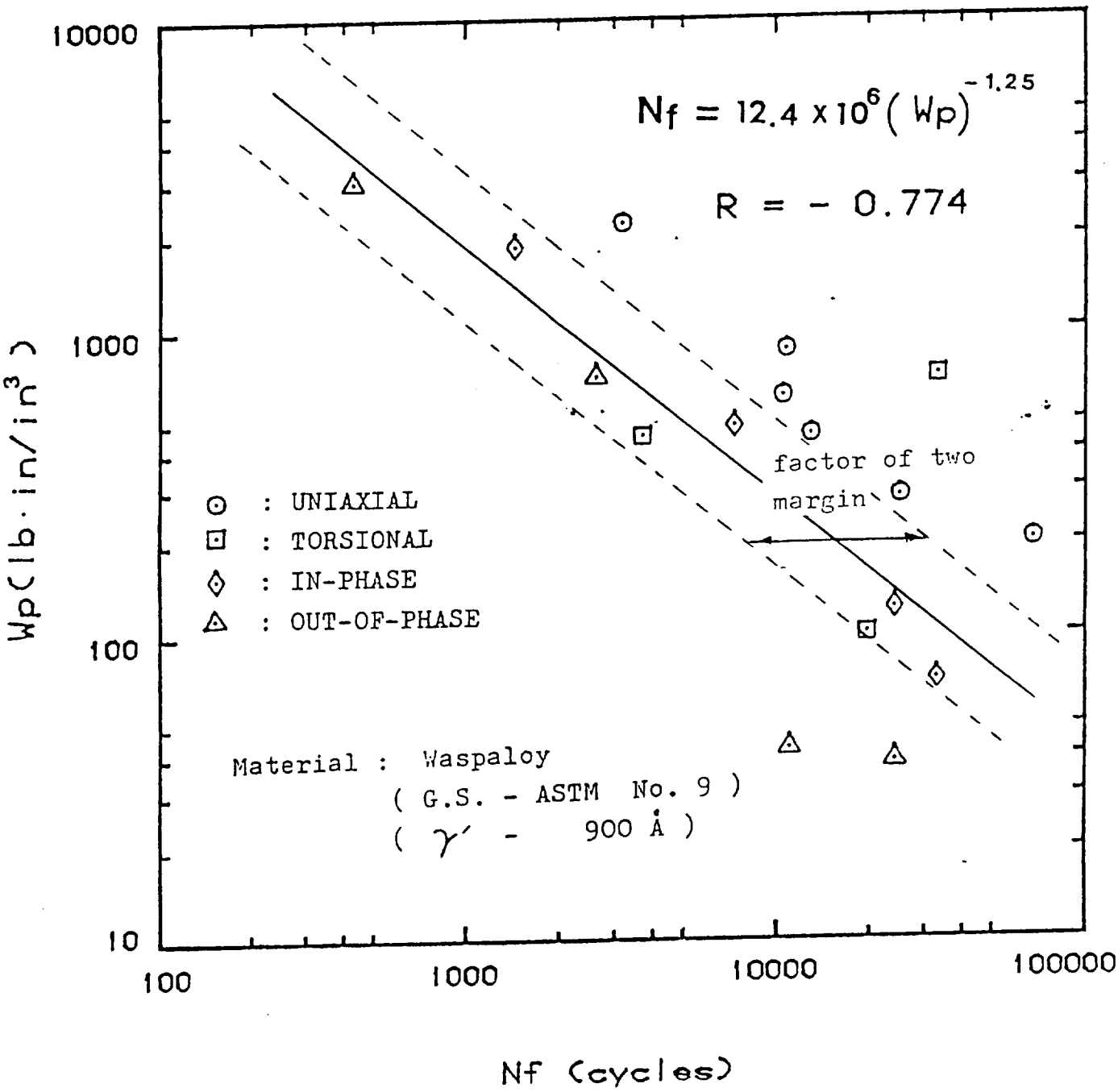
10000
1000
100
10
100
1000
10000
100000
$N_f = 12.4 \times 10^6 (W_p)^{-1.25}$
R = - 0.774
factor of two
margin
⊙ : UNIAXIAL
⊡ : TORSIONAL
◇ : IN-PHASE
△ : OUT-OF-PHASE
Material : Waspaloy
(G.S. - ASTM No. 9)
(γ′ - 900 Å)
Wp(lb·in/in³)
Nf (cycles)

Figure 7(a)

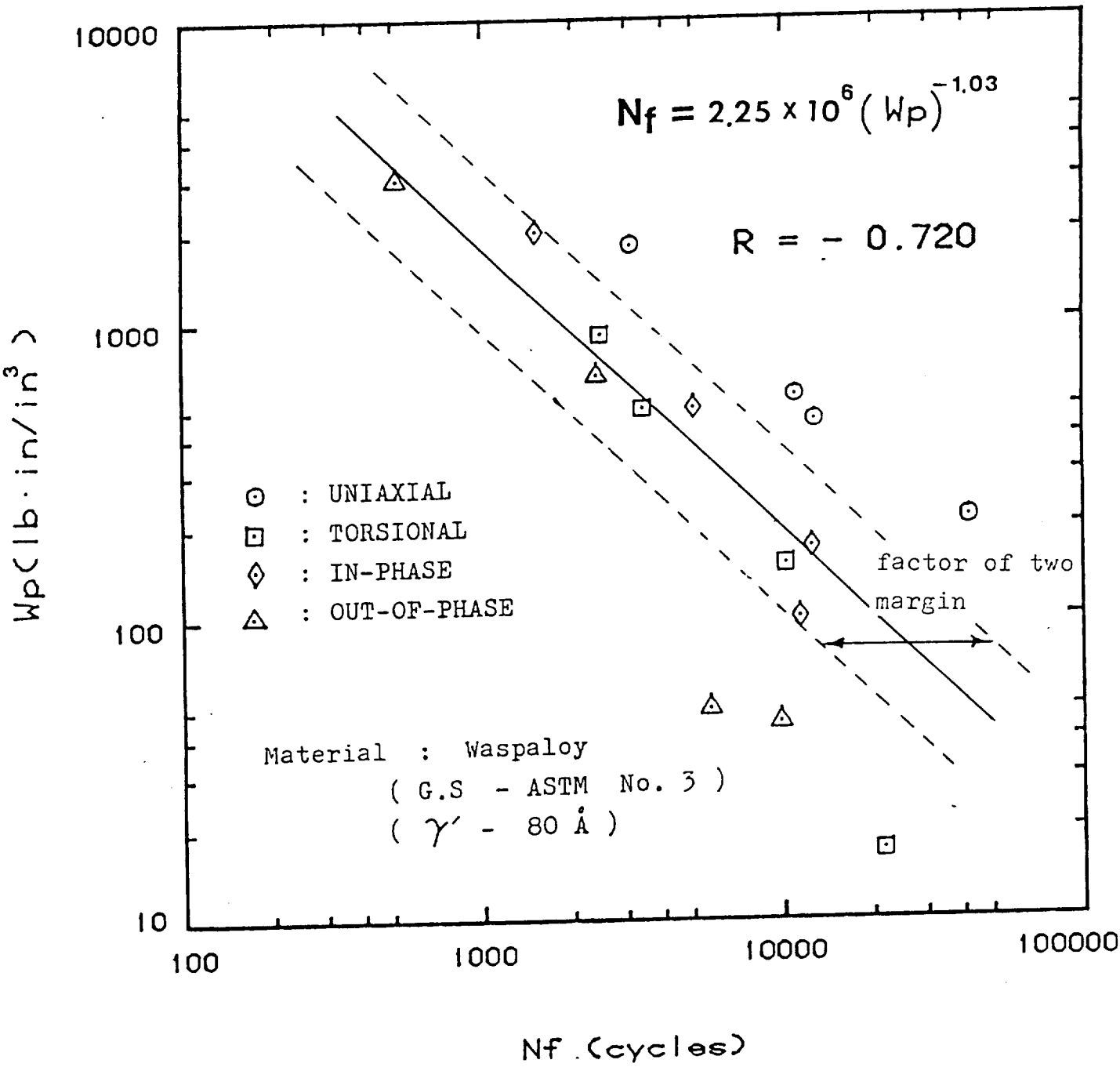
10000
1000
100
10
100
1000
10000
100000
$N_f = 2.25 \times 10^6 (W_p)^{-1.03}$
R = - 0.720
⊙ : UNIAXIAL
⊡ : TORSIONAL
◇ : IN-PHASE
△ : OUT-OF-PHASE
factor of two margin
Material : Waspaloy
(G.S - ASTM No. 3)
(γ′ - 80 Å)
Wp(lb·in/in³)
Nf (cycles)

figure 7(b)

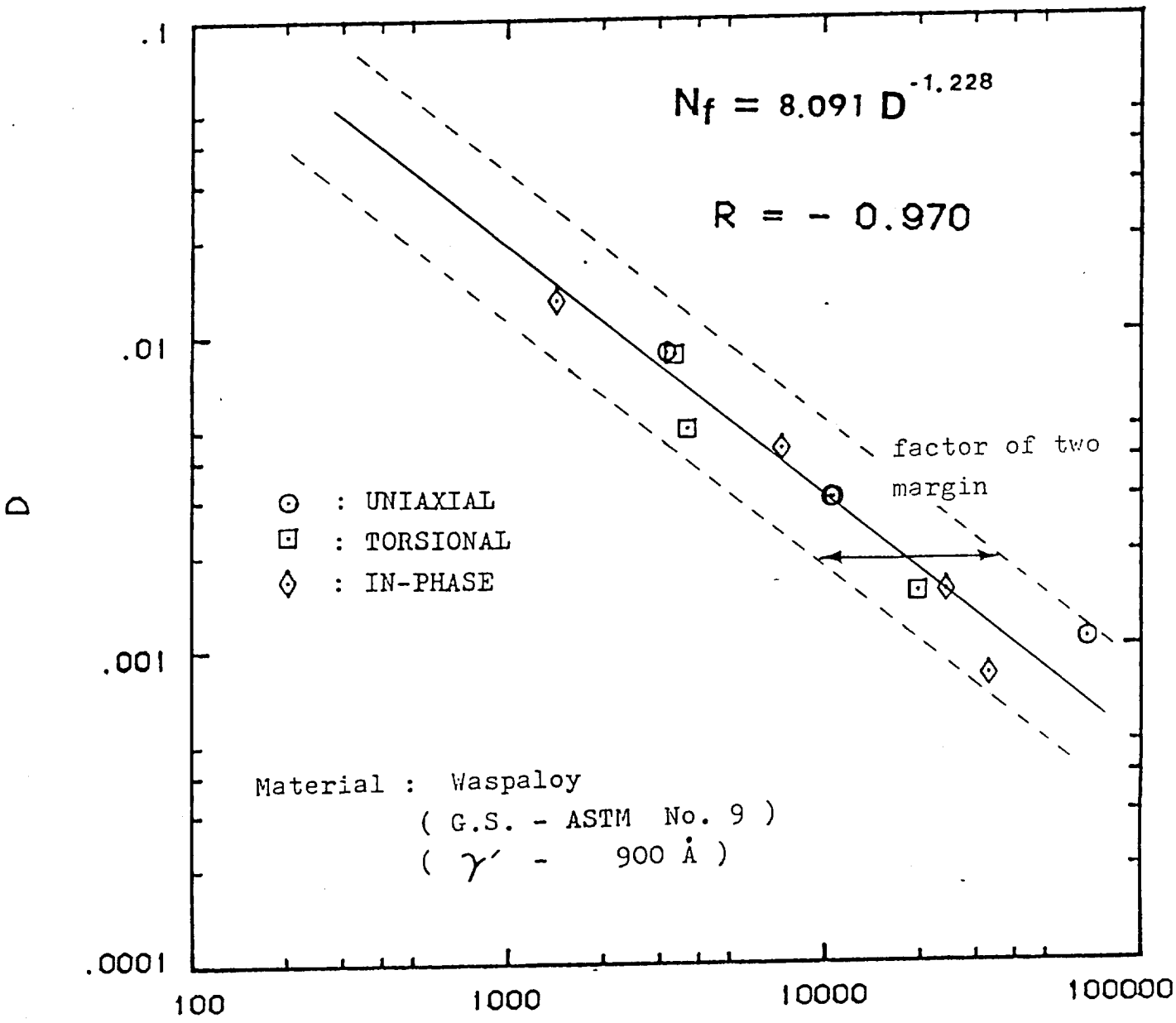
$N_f = 8.091\ D^{-1.228}$
R = - 0.970
factor of two margin
⊙ : UNIAXIAL
⊡ : TORSIONAL
◇ : IN-PHASE
Material : Waspaloy
(G.S. - ASTM No. 9)
(γ′ - 900 Å)
D
.1
.01
.001
.0001
100
1000
10000
100000
Nf (cycles)

Figure 8(a)

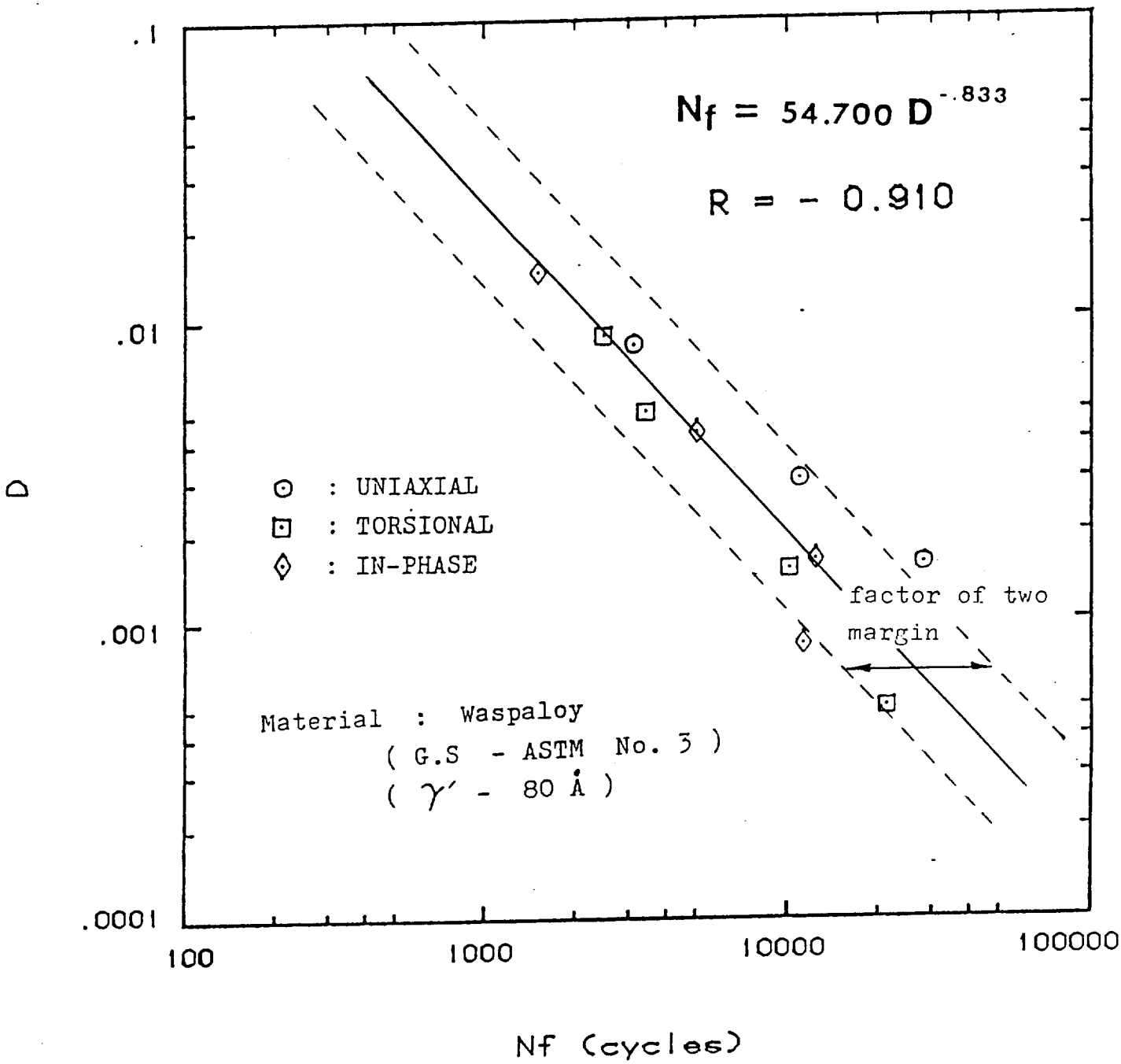
.1
.01
.001
.0001
D
100
1000
10000
100000
Nf (cycles)
$N_f = 54.700\ D^{-.833}$
R = - 0.910
⊙ : UNIAXIAL
⊡ : TORSIONAL
◇ : IN-PHASE
factor of two
margin
Material : Waspaloy
(G.S - ASTM No. 3)
(γ′ - 80 Å)

Figure 8(b)